Published in final edited form as:
NMR Biomed. 2013 July ; 26(7): 810–828. doi:10.1002/nbm.2899.

Nuts and Bolts of CEST MR imaging

Guanshu Liu[1,2], **Xiaolei Song**[2,3], **Kannie W.Y. Chan**[2,3], and **Michael T. McMahon**[1,2]

[1] F.M. Kirby Research Center for Functional Brain Imaging, Kennedy Krieger Institute, Baltimore, Maryland [2] The Russell H. Morgan Department of Radiology and Radiological Sciences, Division of MR Research, Johns Hopkins University School of Medicine, Baltimore, Maryland [3] Cellular Imaging Section and Vascular Biology Program, Institute for Cell Engineering, Johns Hopkins University School of Medicine, Baltimore, Maryland

Abstract

Chemical Exchange Saturation Transfer (CEST) has emerged as a novel MRI contrast mechanism that is well suited for molecular imaging studies. This new mechanism can be used to detect small amounts of contrast agent through saturation of rapidly exchanging protons on these agents, allowing a wide range of applications. CEST technology has a number of indispensable features, such as the possibility of simultaneous detection of multiple “colors” of agents and detecting changes in their environment (e.g. pH, metabolites, etc) through MR contrast. Currently a large number of new imaging schemes and techniques have been developed to improve the temporal resolution and specificity and to correct the influence of B_0 and B_1 inhomogeneities. In this review, the techniques developed over the last decade have been summarized with the different imaging strategies and post-processing methods discussed from a practical point of view including describing their relative merits for detecting CEST agents. The goal of the present work is to provide the reader with a fundamental understanding of the techniques developed, and to provide guidance to help refine future applications of this technology.

This review is organized into three main sections: Basics of CEST Contrast, Implementation, Post-Processing, and also includes a brief Introduction section and Summary. The **Basics of CEST Contrast** section contains a description of the relevant background theory for saturation transfer and frequency labeled transfer, and a brief discussion of methods to determine exchange rates. The **Implementation** section contains a description of the practical considerations in conducting CEST MRI studies, including choice of magnetic field, pulse sequence, saturation pulse, imaging scheme, and strategies to separate MT and CEST. The **Post-Processing** section contains a description of the typical image processing employed for B0/B1 correction, Z-spectral interpolation, frequency selective detection, and improving CEST contrast maps.

Correspondence to: Michael T. McMahon.

CORRESPONDING AUTHOR: mcmahon@mri.jhu.edu.

Supporting Information

A package of Matlab based CEST Data Processing Tools for analyzing CEST data and performing the B_0 correction, CNR filtering, MTR_{asym} map generation, and other tasks described in this review are freely available and may be downloaded through the F.M. Kirby Research Center for Functional Brain Imaging website: http://godzilla.kennedykrieger.org/

INTRODUCTION

Since the term chemical exchange saturation transfer (CEST) was first coined by Balaban and his colleagues at NIH in 2000 (1), this field has quickly attracted broad interest because of its great potential as a new MRI contrast mechanism for biomedical applications. As originally described by Forsen and co-workers (2), the reduction in water signal is generated by applying a frequency-selective saturation pulse (or pulse train) to mobile protons and observing the exchange transfer of signal loss to water. The sensitivity of CEST contrast is much higher than directly observing these protons through MR spectroscopy because the proton signal loss is amplified via many exchange events during the extended period when saturation pulse(s) are applied. Exchange results in transfer of magnetization from the small exchangeable proton pool (e.g. μM to mM range) to a much larger water proton pool (~110 M) until a steady state is reached. Contrary to other MRI contrast mechanisms such as T1, T2, and diffusion weighting, CEST specifically probes molecular targets carrying exchangeable protons in a frequency specific manner, (at the chemical shift of their exchangeable protons) making it a unique technology for molecular imaging. Because of this chemical shift (frequency offset) dependence of CEST contrast, multiple agents possessing exchangeable protons with distinct chemical shifts can be designed such that CEST MRI schemes may detect and discriminate between these agents simultaneously, which has been called multi-color (3-5) or multi-frequency MRI (6,7). This is similar to the most attractive feature found in optical imaging agents, which is difficult to realize with conventional ^{1}H MRI contrast agents. Moreover, when using CEST agents (unlike T1 or T2* contrast agents) all other intrinsic MRI contrasts are perturbed negligibly except in cases where large concentrations of agents collect or when certain CEST agents tuned to produce T2 contrast such as the ones mentioned in the review of Soesbe and coworkers in this issue are used. Also, as we will show later, CEST contrast is favorable at high fields and provides a substantially high contrast to noise ratio (CNR) for biomedical applications, providing an alternative to T1 relaxation contrast agents at high field whose contrast will unfortunately be decreased due to the well-known phenomenon of T1 relaxation time convergence (8).

The difference between CEST and conventional Magnetization Transfer Contrast (MTC) is a question frequently raised. The general consensus is that MTC is a result of magnetization transferring between macromolecules in the solid or semi-solid phase and bulk water through cross-relaxation (9,10) and/or a combination of cross-relaxation and chemical exchange (11,12). Macromolecules possess short T_2 relaxation times (on the order of 10 μsec) (13), much shorter than water in a wide range of tissues or solute protons suitable for generating CEST contrast. As a result of this, their linewidths are much broader than those of CEST protons, on the order of 100 kHz. The saturation lineshape of such a MT pool are approximately symmetric and could be mathematically described by super-Lorentzian (14). While it may be difficult to decouple conventional MTC from CEST effect experimentally at a particular saturation frequency, MTC typically can be observed over a very broad range of frequency offsets, whereas CEST can be only observed at the resonance frequencies of the exchangeable protons in the compound or particle. CEST contrast generally originates from protons on molecules or associated with well-dispersed particles that exchange with

bulk water solely through chemical exchange, and can be in the form of proton exchange (1,5,15-17) (Fig. 1a), water ligand exchange (17-19) (Fig. 1b), a combination of the two (Fig. 1c), compartmental exchange (20-24) (Fig. 1d), or a combination of compartment and proton exchange (25,26) (Fig. 1e). An exception to applying CEST to water exchange has been developed by Pines, Dmochowski and colleagues using Xenon as the solvent (which can be Hyperpolarized to allow sufficient sensitivity for detection) and cryptophan cages as the compartment with a perturbed chemical shift (27-29). CEST agents can also be subdivided into the following classes: diamagnetic CEST (DIACEST), paramagnetic CEST (PARACEST) and hyperpolarized CEST (HYPERCEST) (27).

Based on the advantages mentioned above, there is great enthusiasm within the MRI contrast agent community to develop new and powerful CEST agents and implement these into biomedical applications. One extremely attractive feature of these agents is the potential to be sensor to sense a variety of environmental factors and molecules (1,17,30). For example, pH influences proton exchange rates through an acid and base catalysis of the exchange rate as described in detail by a number of groups previously (31-34). To date, a range of agents have been developed including CEST probes for specifically detecting biologically and pathologically relevant molecules such as: inorganic ions (35-37), glucose/glycogen (38-40), enzymes (41-44), metabolites (45-50), peptides and proteins (5,51-53), nucleoside base (16,44) and temperature (54-56). Biomedical applications which might benefit from CEST imaging include: detecting and grading tumors (53,57,58), characterizing ischemia (45,59), monitoring drug delivery (60) and release (60,61), monitoring cell therapy (36), monitoring osteoarthritis (62-64), and monitoring gene expression (65). Comprehensive reviews of these recent developments and other possible biomedical applications can be found in the review of Terreno and coworkers in this issue and elsewhere (6,66-72).

Many exciting new techniques have been reported to improve the sensitivity, specificity or inter agent discrimination capabilities of CEST imaging because there are a number of technical hurdles when applying CEST MRI to a broad range of biomedical applications. Each application presenting its own set of challenges. These challenges include (but are not limited to): long acquisition times/poor temporal resolution, large RF power deposition, low specificity in the presence of endogenous CEST or MT contrast, and artifacts caused by B_1 or B_0 inhomogeneity. This review will focus on these newly reported techniques and will provide guidance for choosing the best technique for a given agent and pre-clinical or clinical application.

1. BASICS OF CEST CONTRAST

The name Chemical Exchange Saturation Transfer was chosen because the contrast was first observed using the saturation transfer technique, a strategy employed much earlier in NMR spectroscopy (2). While detecting a reduction in water signal produced by saturation pulse(s) is still the predominant method for observing CEST contrast, several alternative methods have been also reported (73-77), and more may be presented in the near future. Therefore, to be more general, CEST is defined as a type of MRI contrast that is created by applying

pulses to exchangeable protons and observing the subsequent alteration in water magnetization. We will first describe saturation transfer in detail below.

Saturation Transfer (ST)

Mathematical Model of Saturation Transfer: CEST contrast is generated in the presence of chemical exchange between solute and solvent provided there is a large enough exchange rate, i.e. on the order of the chemical shift difference between the exchangeable protons and water, and a saturation pulse(s) is applied either on-resonance or nearly on-resonance, with the exchangeable protons which is sufficiently strong to saturate the protons and long enough for multiple exchange events to occur. Multiple mathematical models are available to describe this process and provide guidance for optimizing the contrast. To date, the simplest model is the two-pool model (2,15,78,79). The two pools are the exchangeable proton pool and bulk water proton pool with difference in proton chemical shifts ($\Delta\omega$) and equilibrium exchange rate (k_{ex}). In contrast to the standard model of saturation transfer in NMR where the sizes of two pools are similar, the proton concentration in the water pool (~110 M) is significantly larger than the solute proton pool (~ μM - mM). Hence the equation $k_{ex}= k_{sw}+k_{ws} \approx k_{sw}$ with the relative magnitudes of k_{sw}, k_{ws} determined through mass balance by: $k_{sw} /k_{ws}= M_{0w}/M_{0s}$ where M_{0w}, M_{0s} are the equilibrium magnetizations of water and solute exchangeable protons respectively. The exchange rate, k_{ex}, has to be on the order of $\Delta\omega$ or less. Below $k_{ex} = \Delta\omega$ protons with faster exchange will generally produce larger CEST contrast. This simple two-pool model very often is adequate for interpreting in vitro (78) and even in vivo data (80). One of the advantages of the two-pool model is the possibility of using an analytical solution(15,81), which is simple and easy to use compared to obtaining numerical solutions to the Bloch Equations (79). In particular, the analytical solution for the Proton Transfer Ratio (PTR, CEST contrast) upon application of a saturation pulse is given by:

$$PTR=\frac{S_{0w}-S_w\left(t_{sat},\alpha\right)}{S_{0w}}=\frac{k_{sw}\cdot\alpha\cdot x_{CA}}{R_{1w}+k_{sw}\cdot x_{CA}}\left[1-e^{-\left(R_{1w}+k_{sw}\cdot x_{CA}\right)t_{sat}}\right] \quad [1]$$

in which ^{x}CA is the fractional ratio of exchangeable protons to bulk water protons, t_{sat} is the saturation time, and α is the saturation efficiency defined as

$$\alpha=\frac{\omega_1^2}{\omega_1^2+pq} \quad [2]$$

and

$$\begin{aligned} p &= R_{2s}+k_{sw}-k_{sw}^2\cdot x_{CA}/\left(R_{2w}+k_{sw}\cdot x_{CA}\right) \\ q &= R_{1s}+k_{sw}-k_{sw}^2\cdot x_{CA}/\left(R_{1w}+k_{sw}\cdot x_{CA}\right) \end{aligned} \quad [3]$$

Note that Eq. [1] is equivalent to the expressions reported by Zhang et al. (18) and Aime et al. (17), when the applied RF is strong enough to produce complete saturation (i.e. $\alpha = 1$).

More complicated mathematical models, including three-pool models (79,82-84) and four or higher pool models (85) have also been reported which include additional exchangeable

proton and/or semi-solid proton pools. A number of CEST agents contain multiple types of exchangeable protons, so it is necessary to include these to model their behavior properly. In addition, including exchangeable protons or semi-solid protons in the model is important to understand the *in vivo* CEST data. However, the introduction of additional variables which are often hard to measure experimentally complicates analysis and can preclude their use, even though efforts have been made to derive simplified solutions (82).

Experimentally, CEST contrast is usually determined through collecting a z-spectrum (86), a plot of the normalized z magnetization of water (S_w/S_{0w}) as a function of saturation offset. Fig. 2, which is reproduced from the excellent review paper by van Zijl and Yadav (72), provides a good illustration of how a z-spectrum is plotted to directly visualize CEST contrast. As shown in this figure, a significant reduction in water signal will occur after irradiation at a frequency offset which corresponds to the resonance(s) of the CEST agent ($\Delta\omega$), and in addition a big 'valley' will be present (Fig. 2c) due to direct water saturation (DS), also known as water spillover. When t_{sat} is sufficiently long, the saturation transfer reaches a steady state and Eq. [1] becomes:

$$S_w^{ss}=S_w\left(t_{sat}\to\infty\right)=S_{0w}\cdot\frac{R_{1w}+k_{sw}\cdot(1-\alpha)\cdot x_{CA}}{R_{1w}+k_{sw}\cdot x_{CA}} \quad [4]$$

which can be rearranged into:

$$1-\frac{S_w^{ss}}{S_{0w}}=\frac{k_{sw}\cdot\alpha\cdot x_{CA}}{R_{1w}+k_{sw}\cdot x_{CA}} \quad [5]$$

Eq. [5] can be further simplified to a pseudo-first order equation, as first demonstrated by Ward et al. (1,87) and Goffeney et al. (16) assuming α=1, $R_{1w} >> k_{sw}x_{CA}$.

$$1-\frac{S_w^{ss}}{S_{0w}}=\frac{k_{sw}\cdot x_{CA}}{R_{1w}} \quad [6]$$

The assumptions for Eq. [6] often hold *in vitro*. For example, for a CEST agent with k_{sw} = 100 Hz at a concentration of 30 mM, $k_{sw}x_{CA} \sim 0.027\ s^{-1}$. This is much smaller than R_{1w}, which is typically ~ 0.25 - 0.35 s^{-1} *in vitro*. Hence Eq. [6] can often be used to predict the *in vitro* contrast provided the exchange rate and concentration are known.

Quantification: Perhaps the most straightforward quantification metric for CEST contrast is the PTR (15,78), which is analogous to another metric used in quantifying conventional MTC, the Magnetization Transfer Ratio (MTR). Similarly, the Proton Transfer Enhancement (PTE)(78,87), is defined as:

$$PTE=\frac{k_{sw}\cdot\alpha}{R_{1w}+k_{sw}\cdot x_{CA}}\left[1-e^{-\left(R_{1w}+k_{sw}\cdot x_{CA}\right)t_{sat}}\right]=PTR/x_{CA} \quad [7]$$

Note that PTE (unit=mol^{-1}) reflects the proton transfer efficiency per unit concentration of a given contrast agent and, as a result, is a suitable metric for comparing CEST agents candidates (5).

It is not possible, however, to measure PTR or PTE directly *in vivo* because, as mentioned above, the saturation pulses used to create CEST contrast will also reduce the water signal through DS and MTC. In addition, if a study involves administering an exogenous CEST agent, the endogenous PTR of the tissue imaged should also be considered. Typically, the total saturation of water $S_w(\Delta\omega)^{total}$ can be described by

$$\frac{S_w(\Delta\omega)^{total}}{S_{0w}} = PTR^{exo}(\Delta\omega) + PTR^{endo}(\Delta\omega) + MTC(\Delta\omega) + DS(\Delta\omega) \quad [8]$$

Given the fact that both DS and MTC are approximately symmetric with respect to the water resonance, one can use MTR_{asym} defined in Eq. [9] to separate the CEST effect from MT and DS.

$$MTR_{asym} = MTR^{total}(\Delta\omega) - MTR^{total}(-\Delta\omega) = \frac{S_{sat}(-\Delta\omega) - S_{sat}(\Delta\omega)}{S_{0w}} \quad [9]$$

$$MTR_{asym} = PTR^{exo} + PTR^{endo} \quad [10]$$

As mentioned (Eq. [9]) the assumption of MTC being symmetric with respect to water is true for *in vitro* samples and for PARACEST agents whose offsets are sufficiently far from water resonance. However, as shown by Hua et al (88), this assumption becomes invalid for the frequency range close to the water resonance. This is problematic for most DIACEST and LIPOCEST agents whose offsets are typically less than 5ppm from water. While the apparent MTR_{asym} will be 'contaminated' by asymmetric MTC, this metric is useful to quantify the change in CEST contrast, especially the difference between pre-contrast and post-contrast (51,65), or the difference between target and control tissue (3,40,89), with the assumption that asymmetric MTC is constant. Currently MTR_{asym} is still the most widely used metric for CEST studies.

It should be noted that an alternative definition of MTR_{asym} is in use, and has been shown to be robust *in vivo* by a number of studies(3,45):

$$MTR_{asym} == 1 - \frac{S_{sat}(\Delta\omega)}{S_{sat}(-\Delta\omega)} \quad [11]$$

Using this definition, DS and MTC on the opposite side of water from CEST contrast are included in the denominator, resulting in an MTR_{asym} which is 'normalized' according to the signal losses produced by DS and MTC at -Δω. This definition produces higher MTR_{asym} values than Eq. [9]. The advantage of using this definition is that, assuming the same macromolecular content, the impact of B_1 inhomogeneity can be reduced because, intuitively, an increase or decrease in B_1 will result in a raising or lowering in the denominator through an increase or decrease in MTC. As a result, this new metric is expected to be more accurate for monitoring CEST contrast over time within the same tissue. This definition has been used in the study of monitoring lymphatic uptake of DIACEST liposomes(3), where the CEST contrast of the targeted lymph node is directly

compared to the contralateral node. However, caution has to be used when comparing CEST contrast originating from different tissues because there can be significant differences in DS and MTC of the tissues which will bias comparisons. Other metrics derived from MTR_{asym} have been proposed based on integration (38,90), these will be discussed later in the section on Data processing.

Detectability: Considering detection will be affected by the amount of noise present in the images, the contrast-to-noise ratio (CNR) can provide a better measure of detectability than just assuming $MTR_{asym} \geq 5\%$ will be detectable. Assuming the CEST contrast is generated based on the subtraction of $S^{+\Delta\omega}$ from $S^{-\Delta\omega}$, the CNR can defined as:

$$CNR = \frac{S^{-\Delta\omega} - S^{+\Delta\omega}}{\sqrt{\sigma^2_{-\Delta\omega} + \sigma^2_{+\Delta\omega}}} = \frac{S^{-\Delta\omega} - S^{+\Delta\omega}}{S_0} \cdot \frac{S_0}{\sqrt{\sigma^2_{-\Delta\omega} + \sigma^2_{+\Delta\omega}}} \quad [12]$$

or

$$= \frac{S^{-\Delta\omega} - S^{+\Delta\omega}}{S^{-\Delta\omega}} \cdot \frac{S^{-\Delta\omega}}{\sqrt{\sigma^2_{-\Delta\omega} + \sigma^2_{+\Delta\omega}}} \quad [13]$$

where $\sigma_{+\Delta\omega}$ is the standard deviation of the noise region in the CEST weighted images. Eqs. [12] and [13] indicate that use of either definition of MTR_{asym} will not change the detectability for a given agent.

The lowest detectable concentration is determined by the concentration of agent which produces a CNR= $2\sqrt{2}$, a general threshold which can be applied to *in vivo* studies (91).

Determining k_{ex} for a CEST agent: It is extremely useful to determine the exchange rate(s) for an agent so that one can evaluate it's potential for *in vivo* applications and determine if chemical or physical modifications are necessary. Calculating MTR_{asym} alone is not sufficient for determining this rate, as the concentration of the agent will affect the amount of contrast. It is possible, although challenging, to use more sophisticated imaging sequences to extract concentrations and chemical exchange rates or determine the exchange rate without knowing the concentration.

MRS Measures of Exchange Rate: For high concentration exchangeable protons in the slow exchange regime, exchange rates can be measured directly through spectroscopy by determining their linewidth (*LW*). This is possible because the LW is related to the transverse relaxation rate ($R_{2s}=1/T_{2s}$) and the exchange rate by (92,93):

$$k_{sw} = \pi \cdot LW_s - R_{2s}$$

This approach is generally limited to measuring in vitro NMR samples, due to the concentration and knowledge of R_{2s} requirements. Large contributions to LW from B_0 inhomogeneity will complicate this analysis.

Alternatively, exchange rates can be measured using so-called water-exchange WEX spectroscopy (11,94,95), in which the water magnetization is selectively inverted and subsequently transferred from water to solute within a mixing time (t_m). To determine exchange rates, the signal for exchangeable protons on the solute (S_s) is measured as a function of t_m (15,94) and fit using the expression:

$$S_{\mathrm{s}}(t_m) = \frac{k_{sw} S_{0\mathrm{s}}}{k_{sw} + R_{1\mathrm{s}} - R_{1\mathrm{w}}} \left(e^{-R_{1\mathrm{w}} t_{\mathrm{m}}} - e^{-(k_{sw} + R_{1\mathrm{s}}) t_{\mathrm{m}}} \right) \quad [14]$$

Here S_{0s} is the equilibrium magnetization of solute protons. The advantage of WEX spectroscopy is that when $k_{sw} >> R_{1w}$ and $k_{sw} >> R_{1s}$, substantial errors in R_{1s} and R_{1w} will not produce significant errors in the k_{sw} values determined from the fits. However, this method is less suitable for determining fast exchange rates (k_{sw} ~ 300-400 Hz or higher) because the maximum intensity of the signal is reached at very short mixing times (several milliseconds) which places stringent requirements on the selective water labeling period.

MRI Measures of Exchange Rate: Although the above MRS methods are well suited for measuring exchange rates on a single uniform sample, there are additional challenges posed by measurements on phantoms containing multiple agents and for *in vivo* data where there might be a spatial distribution of exchange rates. To overcome these challenges, MRI approaches have been developed. The first comprehensive techniques that were proposed utilized the t_{sat} or B_1 field dependence of the water signal during saturation transfer imaging, and were termed quantification of exchange as a function of saturation time (QUEST) and saturation power (QUESP) (78). If a CW pulse is used, the z magnetization of water as a function of t_{sat} can be fit using the analytical solution presented in Eq. [1] assuming: 1) $MTR_{asym} = PTR$ as described in Eq. [10]; 2) $k_{sw} << \omega_1$; 3) $k_{sw} << \Delta\omega$; and 4) $\arctan(\omega_1/\Delta\omega) < 30°$. For other cases the Bloch equations should be numerically solved as described in detail in McMahon et al. (78). In this report, both theoretical simulations and experimental data on phantoms (Figs. 3a &3b) showed that k_{sw} can be accurately determined using either the QUEST or QUESP experiments and fitting the data to either analytical or numerical solutions to the Bloch Equations. However, caution has to be taken when performing this experiment for several reasons. The fit parameters should be carefully chosen, as they may greatly affect the accuracy of the results. For example, when R_{2w} is larger than the parameter used, the fitted exchange rate for either QUEST and QUESP will be distorted by direct saturation of water. The choice of saturation power for QUEST (or range of saturation powers for QUESP) highly influences the accuracy of the fitting, and selection of this power or range of powers requires prior knowledge of the approximate range of exchange rate(s). In addition, to improve the fitting in the presence of direct saturation, the fits of both QUEST and QUESP data can be performed using numerical solutions to the Bloch equations (79). As was shown, numerical solutions provide a better estimate of the exchange rate than the analytical solution, particularly when the four conditions mentioned above are not met.

Inspired by this study, several subsequent techniques have been proposed to improve exchange rate estimation through fitting QUEST or QUESP data to alternate analytical expressions. For example, the omega plot method was proposed to determine the exchange

rates of CEST agents without requiring prior knowledge of their concentration (96). In this approach, an alternative form of QUESP, the steady state water saturation S_S^{SS} is plotted in the form $S_S^{SS}/\left(S_0 - S_S^{SS}\right)$ versus $1/\omega_2{}^2$ (Fig. 3c). Based on the two pool Bloch equations and assumptions of negligible direct water saturation and fast exchange rate compared to R_{1w} (i.e. $k_{sw}>>R_{1w}$), the x-intercept of the plot can be shown to be equal to $-1/k_{sw}{}^2$, allowing the estimation of exchange rate without knowing concentration. This approach is potentially useful for directly measuring exchange rates *in vivo*, where the agent concentration is typically unknown, however, the assumptions include negligible DS and MT contrast making this method not suitable in many cases, especially for DIACEST or LipoCEST agents. In another very recent report (97), ratiometric analysis was performed on QUEST data, reducing the dependence of the data on choice of B_1 (Fig. 3d). QUEST Ratiometric Analysis (QUESTRA) normalizes the magnetization transfer ratio at the CEST and reference frequencies, which potentially reduces the dependence of the fits on parameters such as T1, T2, ω_1, and chemical shift compared to MTR_{asym}.

Another new approach for determining exchange rates has been proposed which uses pulsed saturation transfer (98,99). In this approach, oscillations are observed when plotting the CEST contrast as a function of saturation pulse flip angle with the amplitude of the oscillation dependent on exchange rate (whereas variations in other parameters such as T1w and T2w don't affect this amplitude). Because of this dependency, the exchange rate therefore can be determined in an unbiased manner. This multiple flip angle approach may be suitable for studies on a clinical scanner where the use of CW pulses are restricted.

Frequency Labeled EXchange (FLEX)—The FLEX and Exchange Signal Averaging (ESA) sequences are fundamentally different from saturation transfer in that a modulation in water signal is imparted based on an evolution time (t_{evol}) which is similar to the indirect dimensions in multi-dimensional NMR experiments (73,77,100). These methods aren't technically CEST methods, as saturation transfer is not employed, however they fall under the CEST imaging umbrella as they are methods which allow the collection of images with the contrast in these images dependent on chemical exchange. A figure describing the differences between the FLEX experiment and saturation transfer is given below (Fig. 4). The main element of the sequence is a succession of identical Label Transfer Modules (LTMs), which create the modulation in water signal, through a systematic variation in t_{evol} across the series of images collected, and post-processed. Current implementations rely on keeping the total time of each LTM constant for all evolution times collected in the series, although this is not a requirement of the sequence. The signal generated for each pixel can be described via a free induction decay (FID), and converted from the time domain into the frequency domain via fourier transformation as shown in Fig. 4a. FLEX and ESA are similar to saturation transfer in that the preparation of magnetization can be placed in front of many image acquisition schemes. There are multiple advantages to these sequences, as will be discussed later. These schemes have different requirements in total scan time from saturation transfer as the number of images collected is adjusted to adequately sample the time-domain of the preparation module as well. The number of points and t_{evol} used in sampling have to be optimized based on the chemical shift of the CEST agent protons, their chemical

exchange rate, and the offset of the labeling pulses. As has been demonstrated (73), analysis of the LTM dependence of the FLEX transfer allows determination of exchange rates in a similar manner to QUEST or QUESP.

2. IMPLEMENTATION

Choice of magnetic field—Increasing the magnetic field strength (B_0) can substantially increase the sensitivity of the signal on MRI scanners (8), which has led to the development of commercial MRI scanners with high and ultra high magnetic fields in the last decade, both for humans (up to 11.7 Tesla) and animals (up to 21 Tesla). MR parameters will change as a function of B_0, which has been termed field dispersion. The T1 and T2 of cortical tissue of mice at different field strengths are displayed in Table 1, which are important to CEST contrast. In contrast to T1 and T2* contrast agents, CEST agents are suitable for high fields and could play an important role on high field strength scanners. The reasons for this are: 1) the separation of exchangeable protons from water ($\Delta\omega$) is proportional to the main field strength. A larger $\Delta\omega$ will allow the use of CEST agents with faster exchange rates without the concern of violating the slow to moderate exchange rate restriction ($\Delta\omega \geq k_{sw}$); 2) The longer T1 relaxation times at high field will slow down the recovery from saturation, resulting in a larger CEST contrast. The dependence of CEST contrast with B_0 can be predicted using numerical simulations. As shown in Fig. 5, based on the published relaxation times MTR_{asym} is proportional to the B_0 field strength for all the exchange rates tested, especially for $B_0 < 9.4T$. However, the specific absorption rate (SAR) of RF power increases approximately with the square of the field strength (101), which may also result in an inability to capitalize on this dependence.

Choice of imaging pulse sequence—The current paradigm to create CEST is through application of long saturation pulses or pulse trains (i.e. > 2-3 seconds). If this long preparation period is implemented prior to each collection of points in k-space (17), the acquisition time can become impractically long. For example, using a standard fast spin echo sequence with a TR of 3 sec to allow the saturated protons to recover prior to the next scan (t_{sat} = 2 sec), the total acquisition time is approximately 9.6 minutes to acquire the minimal set of three images needed for CEST imaging: S0, S(+$\Delta\omega$), and S(–$\Delta\omega$) with each acquired using 64 phase encoding steps. For practical collection schemes therefore it is necessary to utilize fast imaging sequences to accelerate CEST acquisitions to an acceptable temporal resolution. This is particularly important for dynamic contrast investigations which often require temporal resolutions on the order of one minute or less.

As first demonstrated by Liu et al. (91), two possible strategies can be used to improve the temporal resolution of collecting CEST images through fast imaging pulse sequences : 1) a multiple echo/steady-state sequence strategy, or 2) a fast gradient echo sequence (e.g. FLASH) (Fig. 6). Using either of these two strategies, or a combination (102), the acquisition time is reduced significantly without compromising the CEST contrast. To date, CEST images have been collected using a variety of fast imaging sequences, including: EPI (51,52,102), RARE (3,44,91), FLASH (91), FISP (38) and GRASE (103). Table 2 summarizes the features of each method and therefore provides practical guidance.

In practice, the appropriate pulse sequence should be chosen, in addition to the acquisition speed, by the characteristics of each pulse sequences including if it is suitable for a given B_0 field strength, anatomical region, if the SNR will be adequate and if specific absorption rate (SAR) will be an issue. For example, while the RARE sequence has been widely used and produces exquisite images at high field, the additional refocusing pulses can create SAR concerns on clinical scanners. Gradient echo sequences, on the other hand, have the advantage of low SAR and high speeds, but can produce poor quality images because of eddy currents and B_0 inhomogeneity, limiting their application at high fields (i.e. ≥ 7T).

For PARACEST agents, ultrashort TE methods may improve the CEST detection as is discussed in detail by Soesebe and coworkers in this issue. Another interesting imaging sequence that has been demonstrated by Ling et al (104,105) is to use the intermolecular multiple-quantum coherence (iMQCs) filter to enhance the exchange contrast. When only the intermolecular double-quantum coherences (iDQs) were selected, the CEST contrast of GAG was enhanced as demonstrated on phantoms, however, at the expense of a significantly decreased SNR.

Choice of saturation pulse(s)—To date, a long, continuous wave (CW) rectangular pulse is the most widely used saturation pulse for CEST MRI, which provides several advantages. For example, the long rectangular pulse is very efficient, allowing a rapid and complete saturation of the solute protons (106). In addition, the Bloch equations using a rectangular CW pulse are simple, resulting in fast computation of numerical solutions and straightforward optimization of CEST contrast since only two parameters, saturation power (B_1) and saturation time (t_{sat}), are adjustable (78). For a CEST agent with exchange rate constant k_{sw}, the optimal B_1 was predicted to be $k_{sw}/2\pi$ using this pulse (79). In addition, the CEST contrast is relatively insensitive to B_1 around the optimal value. However, proper selection of B_1 must also consider the contrast-to-noise ratio (CNR), especially when a stronger B_1 is used, as the strong pulses can increase DS and MTC signal losses which reduce the effective size of water pool that can exchange with solute protons (72). Sun et al. (81) showed that the relationship between CEST contrast, DS and B_1 can be described using an analytical solution to the Bloch equations. Using this equation, the optimal B_1 for obtaining maximal PTR for PLL (B_0=4.7 T) is predicted to be 2.43 μT, which is in accordance with the experimental 2.5 μT. This optimal B_1 is not dependent on the concentration of CEST agent. While this equation is complicated by the number of parameters including pool size ratio (x_{CA}), it can be simplified into three main components: ideal PTR, saturation efficiency (α) and spillover factor (σ) (80,107). The optimal B_1 is achieved through balancing saturation efficiency and spillover. However, this expression's flaw is that it neglects MTC, which must be taken into account for *in vivo* CEST imaging. As shown in a recent study (83), choosing a lower B_1 can be favorable for detection of CEST contrast because MTC is reduced. As a result, typically B_1 is optimized experimentally for each new *in vivo* application.

Despite the wide use of long rectangular CW pulses in CEST imaging, clinical translation of CEST imaging using such pulses can be problematic as the field strength of the saturation pulses will be limited by SAR concerns. The exact field strength allowed is a complicated question, as SAR will also be affected by the choice of transmit coil and use of smaller

transmit coils (108) or parallel transmit coils (109) can reduce the deposition of heat. However, in the case that the hardware doesn't allow sufficiently strong cw pulses for saturation, an alternative is to use a train of shaped pulses instead (110), often called pulsed-CEST MRI. A number of waveforms have been tested which were previously used in NMR spectroscopy and conventional MTC studies including: Fermi (96,111), e-burp (67,112), Gaussian (50,113), SEDUCE (110), d-SNOB (110), and Blackman-shaped inversion pulses (114). Simulations were performed to illustrate how to choose the waveform and settings that should be used for CEST studies (Fig. 7). The calculations were performed using the program SPINEVOLUTION (115) using the chemical exchange library recently added to this software for a phantom at 11.7T with a contrast agent which has $\Delta\omega$ = 5ppm, k_{sw} = 1000 Hz (similar to the CEST agent barbituric acid). In Fig. 7a, the most common shape, a long rectangular CW pulse, is shown. As is shown in Fig. 7b, applying saturation pulses shorter than 5s results in substantial wiggles around the water frequency at this saturation field strength. It is important to keep in mind that the conditions required to avoid these wiggles varies with saturation field strength with imaging gradients potentially suppressing them. These wiggles can be eliminated using weaker saturation fields even if the t_{sat} is short,. For example, use of t_{sat} = 2 sec is sufficient when B_1=3.6 μT, and use of t_{sat} = 0.5 sec is sufficient for B_1= 0.5 μT. The challenge of choosing pulsed saturation instead and an alternative waveform is that optimization is more complicated and these trains can have a tendency of generating wiggles in the z-spectrum. Several additional parameters need to be added into the theoretical model which affect the performance of these shaped pulses or pulse trains: saturation pulse duration (τ_p), inter-pulse delay time (τ_d), the pulse shape defined by the time-dependent B_1 function B_1 (t), and the number of pulses (n). In addition, there are two dependent parameters: flip angle of saturation pulse (θ), which is defined by the net effect of RF pulse on a spin over the period of τ_p, and duty cycle which is defined by τ_p /(τ_{p+} τ_d). Fig. 7 shows two alternative shapes which have been used previously, dSNOB (110) (Fig. 7d-f), and Fermi(96) (Fig. 7g-i). As shown in Fig. 7e, setting τ_p = 5 ms, τ_d = 0, θ =180° for dSNOB pulses produces similar z-spectra to the rectangular pulses, with a reduction in the number of wiggles, but broader and steep features in both water dips and CEST dips at 5 ppm from Fig. 7b. Fig. 7h shows some of the complications of choosing a Fermi pulse shape. Setting θ =1620 ° produces better results than θ =180 ° for this shape with peak field strength of 3.8 μT (upper panel). Using θ =1620 ° results in smooth Z-spectra at shorter t_{sat}, (lower panel) with the efficiency slightly reduced from Fig. 7b.

Sun et al. (116) derived a simplified expression to optimize conditions for pulsed-CEST acquisition. Such an approach, as indicated by the authors, is only suitable for certain pulse shapes. Zu et al. (84) derived an alternate expression based on the average B_1 power ($B_{avg\ power}$) which includes two parameters describing the shaped pulses:

$$B_{avg\_\,power}=\sqrt{\frac{1}{(\tau_P+\tau_d)}\int_0^{\tau_P} B_1^2\,(t)\,dt}=\frac{\pi\theta}{180\cdot\gamma\cdot p_1}\cdot\sqrt{\frac{p_2}{(\tau_P+\tau_d)\cdot\tau_P}} \quad [15]$$

where p_1 is the ratio of the average amplitude to the maximum amplitude and p_2 is the ratio of the average of the square of the amplitude to the square of the maximum amplitude respectively for the shaped pulse. p_1 and p_2 are well defined for a specific shape, for

example, p_1= 0.416, p_2 =0.295 for the Gaussian pulse used in their study. The optimal $B_{avg\ power}$, is still approximately the same whether shaped pulses or long rectangular are used for saturation. In addition, this study indicated that one should use the maximum allowed duty cycle since increasing the duty cycle increases the efficiency of CEST contrast generation.

More exotic types of preparation schemes have also been tested. Several groups have investigated applying saturation pulses with the frequency or phase alternated systematically within the pulse or pulse train which includes:z-spectroscopy with Alternating-Phase Irradiation (ZAPI) (117), Saturation with Frequency Alternating RF Irradiation (SAFARI) (114), Two-Frequency irradiation (118), and WALTZ-16* composite pulses for On resonance PARAmagnetic Chemical Exchange Effects (OPARACHEE) (119,120). Alternatively, the magnetization can be prepared prior to application of long saturation pulses to impart T1rho contrast (75) or Positive contrast (74). Some of these strategies appear to be promising for discriminating MTC from CEST contrast as will be discussed later in the **Strategies to separate MT and CEST** section.

Choice of imaging scheme

Alternatives to full z-spectral acquisition: In practice, researchers are often only interested in determining the CEST contrast at one particular offset instead of examining the whole z-spectrum. Of course, image collection would be much faster through a two-offset (+Δω and -Δω) saturation scheme, which can be sufficient when the saturation field strengths used is strong relative to the B_0 inhomogeneity (91,121,122). For detecting DIACEST or LIPOCEST agents, particularly outside the brain, multiple offsets around +Δω and -Δω should be collected which span the range in B_0 shifts detected in the B_0 maps to properly correct MTR_{asym} maps. For example, Zhou et al. (123) demonstrated that a six-offset acquisition scheme (Fig. 8) was sufficient for acquiring high SNR APT images of brain tumors in patients. This scheme was short enough to be performed in a clinically relevant time frame (~ 2.8 min or 4.5 min with a low SNR z-spectrum for assessing B_0 inhomogeneity ~1.7 min). Depending on the shimming conditions, this six-offset imaging scheme can be sufficient for detection of CEST contrast agents in subcutaneous tumors as well. Alternatively on resonance approach could be used without the need of multiple chemical shift selective saturation pulses. For instance, it was shown that a low power WALTZ-16* preparation pulse could be used to create detectable CEST contrast using the OPARACHEE scheme(124). Images collected using this method often possess low SNR due to the large amounts of signal loss generated by the WALTZ-16* preparation. In addition, this method lacks the capability of discerning CEST contrast from conventional MTC. Other alternatives include the LOVARS (125), and SAFARI (114) schemes which will be described in the **Strategies to separate MT and CEST** section.

Strategies to reduce the number of sampling points in k-space: After selecting a fast imaging sequence, the temporal resolution can be improved further through selection of a suitable k-space sampling trajectory and compressing the sampling of this trajectory. One unique feature of k-space data is that the low frequency data points determine the signal density of an image and the data is symmetric around the center of k-space. Hence,

undersampling k-space using strategies such as asymmetric half-Fourier acquisition (126), keyhole acquisition (127,128) or compressed sensing (CS)(129) can allow a reduction in acquisition time without significantly compromising CEST contrast and enable the quick acquisition of z-spectral data or dynamic monitoring of CEST contrast. These approaches are currently in use in our center and elsewhere (62). For example, Varma et al. recently evaluated the potential of using the keyhole technique for gagCEST measurements (62), where low resolution dynamic data was collected in combination with a high resolution reference image acquired with the same field of view but a larger matrix size. In this report, they found that an undersampling factor of 4 could be used without significant compromising the CEST contrast. However, caution has to be taken using these approaches because undersampling will result in lower SNR and may also lead to de-emphasizing signal changes confined to small regions.

Strategies to suppress fat artifacts: The use of fat suppression in the CEST pulse sequence is required if a non-negligible amount fat is present, as fat will generate well-known chemical shift artifacts and also complicate analysis of CEST images due to the lack of exchange contrast on the fat protons in a voxel (130). Even worse, due to the short T1 and long T2 of fat tissue, it will appear bright when Fast Spin Echo sequences are used, potentially compromising the dynamic range of the receiver and affecting the measurement of water signal loss. One strategy is to use a chemical-shift-selective refocusing pulse and crusher gradients to suppress fat signal from spin echo based CEST images (130). Another strategy is to add a short chemical shift selective fat suppression pulse after the long saturation pulse to remove the fat and improve the quality of CEST images(3). Unfortunately, this strategy is vulnerable to B_0 inhomogeneity. Many other techniques can be employed as well.

Volumetric CEST acquisition: Because of the presence of the long saturation pulse or pulse train (on the order of several seconds) single slice acquisition is still the standard approach for many current pre-clinical studies, although not desirable for clinical translation. It is possible to include the RF saturation pulse or pulse train directly in front of a full 3D or a multi-slice imaging sequence in order to collect volumetric CEST measurements. However, as shown by Sun et al.(102) and Liu et al. (91), CEST contrast decays over time after the removal the saturation pulse based on the T1 relaxation time. Consequently, volumetric CEST contrast images must be corrected in post-processing, based on prior knowledge of T1 as well as the details of the k-space trajectory (102). Despite the success in pH measurements on rodent stroke models, the application of this approach might be restricted to cases employing low saturation field strengths (0.5- 0.75 μT). Very recently, Zhu et al.(103) demonstrated that this loss of CEST contrast resulting from T1 relaxation can be minimized using fast 3D sequences such as Gradient and Spine-Echo readout (GRASE). As demonstrated by the authors, the contrast loss was kept minimal and not dependent on the number of slices due to the use of a 3D k-space acquisition scheme where the center of k-space was acquired prior to loss of contrast due to T1 relaxation would occur. As the signal intensity in an image is mainly determined by the center of k-space, this strategy was shown to be successful. All the high frequency k-space data is collected later in a way to uniformly contribute to each slice and limit the effect on the CEST contrast. This

approach allows sensitive 3D CEST image collection within 10 minutes for a 26-offset z-spectrum with the aid of SENSE accelerations in both phase and slice encoding directions. As they showed, properly combining parallel imaging hardware with 3D k-space sampling strategies can allow volumetric CEST measurements.

Another alternative is to employ steady state methods to build up CEST contrast throughout the volume, which has been demonstrated on both 1.5T (111) and 7T scanners (131,132). This approach uses a repetitive element that includes a short saturation pulse in front of each slice selective pulse followed by a fast imaging sequence with a short enough repetition time to allow a build-up in saturation contrast. In one interesting study (133), Sun et al. developed relaxation-compensated imaging scheme using an unevenly segmented RF pulse train, which can be considered as hybrid method combining the two approaches described in Fig. 6, where initially a long saturation pulse train is used to reach a steady state in saturation contrast and afterwards short pulses are used to compensate for loss of CEST contrast due to acquisition time. While this approach is expected to provide similar contrast to single slice measurements, it might not be a time-efficient method because of the extra time required for the compensating saturation pulses in addition to the primary saturation pulse. For example, a number of 0.5 sec secondary pulses were used in this study, in conjunction with a 5 sec long initial saturation pulse. In addition, extra effort is needed to optimize the compensating saturation pulses, including determining the optimal amplitude, duration and excitation flip angles.

Strategies to separate MT and CEST

Saturation Pulse Modulation (Frequency and Phase) Based Methods: Saturation pulses can include modulations to separate MT contrast from CEST contrast. In 2010 the Z-spectroscopy with Alternating-Phase Irradiation (ZAPI) (117) pulses were introduced for separating different contributions (DS, MTC and CEST) to total water signal loss based on the T2-selectivity of the saturation pulse with modulation frequency Ω. They proposed two kinds of modulated saturation pulses: ZAPI with the phase of the square pulse modulating by 180° every 1/ Ω sec, and ZAPISM (Z-spectroscopy with Alternating-Phase Irradiation and Sine Modulation) with the phase alternating and the amplitude sine-modulated. Signal losses due to DS and other long T2 components were eliminated from the central region of the resultant z-spectrum, which allowed the highlight of the saturation of short T2 components (MTC). The DS dips were modulated to the frequencies at ± N*Ω (N=1 for ZAPISM). They suggested that the T2 selectivity in the z-spectrum was strongly related to the modulation frequency Ω allowing the probing of pools with different T2s through varying Ω. Lee et.al (118) further investigated using these sine or cosine modulated, two-frequency saturation pulses. Using Provotorov thermodynamic theory they demonstrated on a liquid-crystalline phantom, that these two-frequency pulses produced a uniform saturation on strongly coupled spin systems (134). As a result, they proposed a new asymmetry analysis with respect to the water frequency, which potentially allows one to isolate CEST contrast from asymmetric MT contrast due to the uniform MTC over a broad range of frequencies. However, the value of this approach needs further testing *in vivo*.

Another two-frequency irradiation scheme for separating MT and CEST has been developed, SAFARI (114), which uses either a pulse train with alternating frequencies of $+\Delta\omega$ and $-\Delta\omega$ or later a cosine-modulated dual-band CW pulse similar to Narvainen et al. (117) and Lee et al. (118) with $\Delta\omega$ equal to Ω. In addition to collecting an image with either of the above modulated saturation pulses, this approach also acquires two images with saturation frequencies of $+\Delta\omega$ and $-\Delta\omega$ using either pulse train or a long rectangular saturation pulse, which are then subtracted to produce a new asymmetry map, the MTR_{SAFARI} map. There were two issues with this experiment, 1) the two-frequency saturation images can have low SNR and 2) it can be challenging to produce equivalent saturation field strengths using one and two-frequency saturation pulses.

Time Domain Based Methods: The conventional schemes for CEST contrast detection and analysis are mostly based on saturation offset incrementation (z-spectrum) and asymmetry analysis. This analysis doesn't remove all CEST contrast map artifacts from spatial B_0 inhomogeneity, particularly in regions with rapid changes in tissue susceptibility compared to the image resolution where partial volume effects complicate the fittings. When large differences in direct water saturation are present in a voxel, the corrections are imperfect, as can be the case at the edge of the brain for example. Also the contrast maps can possess low CNR and image collection times can be long. These remain big obstacles for widespread adoption of the technology, especially for DIACEST and LIPOCEST. Based on the amplification mechanism of CEST imaging that the contrast builds up as t_{sat} increases, CEST contrast can also be detected and characterized using time-domain analysis based methods(73,125,135,136). For example, Song et al. developed a new time-domain CEST mapping method, termed “Length and Offset VARied Saturation” or “LOVARS” (125) (Fig. 9) based on both the Length (t_{sat})-dependence and asymmetric (around water) Offset-dependence of CEST contrast. In this method, a set of images is acquired with systematic variation of the saturation parameters across this set to modulate CEST and other saturation transfer contrasts (e.g. DS, MTC) into different frequencies and phases. Either fast Fourier transform or the general linear model (a widely-used algorithm in fMRI(137)) can be directly employed to analyze and decompose the LOVARS modulation patterns into separate sources of water signal loss. After transformation, a “LOVARS phase” map is generated, which is insensitive to B_0 inhomogeneity. Another advantage of this method is the B_1 dependent saturation efficiency (α) of PTR in Eq.[1] allows the correction of B_1 inhomogeneity through analysis of the ratio of contrast at different T_{sat} (99,128). As has been shown including on live mice bearing 9L gliosarcomas, the LOVARS phase mapping method has a more than four times higher CNR efficiency and exhibits less B_0 artifacts compared to using saturation offset increment based correction to produce conventional MTR_{asym} map. However, these phase maps are also less sensitive to concentration of CEST agent or chemical exchange rate

The FLEX and ESA methods mentioned above are also a time-domain analysis based methods, which employ a series of label-transfer modules (LTMs) to selectively label the exchangeable solute protons and subsequently transferred to water. The water signal is modulated as a function of evolution time due to exchange transfer, which can be reconstructed by FFT as a free induction decay of the amplitude of water signal. Prior to

FFT, time domain analysis on the FLEX FID offers the possibility of removing rapidly decaying components such as semi-solid protons (short T2*) through fitting and then subtracting these components out (100), instead of fitting these features out using the frequency domain analysis methods (MTR_{asym}) widely used in saturation transfer. Another advantage appears to be the feasibility of detecting faster exchange rates than detectable using saturation transfer (135). However, further work is required on this sequence to overcome several technique hurdles such as the high power deposition of this approach, the complexity of the fittings, and the large number of images required for analysis.

3. POST-PROCESSING

The most common procedure for processing CEST imaging data is illustrated in Fig. 10 (138). This procedure includes measuring B_0, correction of the z-spectrum voxelwise through interpolation, and generating MTR_{asym} map(s) at the offset(s) of interest. These steps are described in detail below.

B_0/B_1 correction—One of the most important steps, especially for DIACEST agents, is the need to accurately measure the B_0 for each voxel (generating a B_0 map) and use it to correct the artifacts in CEST contrast maps caused by B_0 inhomogeneity. One way to generate B_0 maps is directly using the z-spectrum by either interpolating or fitting the normalized water signal (S/S0) for each voxel to find the offset corresponding to the strongest saturation. This approach works well if the central peak in the z-spectrum is sharp (a relatively weak saturation field strength used, i.e. < 2μT), or if the CEST agents exchangeable protons are sufficiently far from water so that small errors in B_0 correction won't cause problems (MTC and DS contrast are small)(139). B_0 maps based on these profiles can be distorted because the signal losses due to MTC are asymmetric. For other conditions a separate measurement of the B_0 map has to be be made. One option is to collect gradient echo based phase maps to provide B_0 maps for correcting CEST contrast maps (140). One disadvantage of using phase-mapping based B_0 map, however, is the need for co-registration if a different pulse sequence is used for acquiring B_0 maps than that for z-spectrum. Another concern is that B_0 shifts can be potentially underestimated due to the problem of phase aliasing, in which phase is always wrapped into the interval of [-π π] radians (141,142). To overcome these challenges, a second method, WAter Saturation Shift Referencing (WASSR) (143) has been proposed which involves collecting a second set of images using weak saturation pulses so that the signal loss is predominantly due to DS. In practice, the assumption of signal losses produced mostly through DS can be fulfilled using a CW pulse at ~ 0.5 μT, t_{sat} ~ 500ms (144). The original method employed a non-model based maximal symmetric fitting algorithm. More recently, Liu et al suggested that using a Lorentz lineshape fitting algorithm would be more robust(4), especially at high fields (e.g. 9.4T) where the B_0 inhomogeneity can be > 200 Hz(3). In this case, the lineshape of water DS profile, or the longitudinal magnetization $\left(S_Z^{SS}\right)$, is given by:

$$S_Z^{SS} = \frac{S_Z^0}{1+\left(\frac{\omega_1}{\Delta\omega-\Delta B_0}\right)^2\left(\frac{T_1}{T_2}\right)} \quad [16]$$

Here S_Z^0 is the initial longitudinal magnetization, ω_1 is the strength of the applied RF pulse which is resonating at $\Delta\omega$ (frequency with respect to the proton center frequency), and ΔB_0 is the B_0 shift. The assumption of Eq. [16], $1/T_2 << \Delta\omega$, is generally satisfied for CEST contrast measurements at high field. Fitting the experimental data of S_Z^{SS} at different $\Delta\omega$ allows accurately determining of ΔB_0, and a B_0 shift map is generated pixel-wise.

In addition to B_0 correction, more attention has been paid to B_1 correction recently, especially with respect to translation of CEST technology to high field clinical scanners. Nevertheless, quantitative correction of B_1 inhomogeneity in CEST contrast is challenging(140). An empirical approach has been reported recently to improve measurement of CEST contrast in the presence of severe B_1 inhomogeneity (145). In this approach, B_1 field maps were measured using a double angle method (30° and 60°), which were used to correct the MTRasym maps at the frequency of glutamate using a calibration curve described by a second order polynomial. It was indicated in this report however, that accurate determination of the calibration coefficients highly depends on the saturation and imaging parameters and the type of tissue.

Interpolation of z-spectra—After the B_0 map is determined, the z-spectrum of each pixel is shifted to move the center back to 0 Hz. In order to determine the signal at the offsets of interest, the data set will be interpolated into a new set of data corresponding to the offset(s) of interest using data processing tools such as MATLAB, IDL or Python. A simple spline interpolation (in MATLAB) often works well, especially when the SNR is sufficient so that the Z-spectrum for each pixel is smooth. As we have demonstrated (4), this simple and fast approach is quite suitable for characterizing CEST agents in vitro, even in the presence of B_0 shifts > 500 Hz. However, in vivo CEST MRI requires more sophisticated post-processing as the images generally have lower SNR (i.e. SNR_0<100) and can contain motion artifacts. For example, Zhou et al. have used 12th-order polynomial for fitting z-spectrum and interpolated it into a Z-spectrum with 1Hz resolution (52). Stancanello et al. showed that using a smoothing spline based algorithm could significantly compensate the noisy z-spectrum(139). These interpolation based methods are time-efficient and don't rely on the determination of many parameters, but have the limitation that all the collected data don't contribute to the Contrast to Noise Ratio (CNR) of the CEST contrast maps. Model based fitting methods would be of great interest in the hope of allowing more frequencies to contribute to the CNR, especially for in vivo data where fat artifacts and cross-relaxation may also contribute.

For a tissue or compartment whose relaxation times are similar to free water, the saturation profile is well described using a Lorentzian line shape (146). As a result, the z-spectrum in these tissues can be modeled using two separate components: DS and CEST. Fitting the experimental data to a Lorentzian curve given using Eq. [19] will allow the extraction of the DS component, producing a new z-spectrum without CEST. Consequently CEST contrast is determined by comparing the difference between the experimental z-spectrum and the DS only z-spectrum. This is the case when MTC is negligible such as in aqueous phantom samples (50) or tissues irradiated with a low saturation power(132). It is worth noting that the CEST solute protons can also be considered as a liquid pool, and described by a

Lorentzian line shape (50). As an extension of Lorentzian fitting of CEST, Zaiß et al. (147) recently proposed, based on simulations, to model and separate CEST from MT using a combination of CEST contrast modeled by a Lorentzian and MTC modeled by a Lorentzian under the weak-saturation-pulse (WSP) approximation. In another recent study (148), an analytical solution to the Bloch-McConnell equations was presented for HyperCEST experiments which allows use of Lorentzian line shapes for z-spectral analysis.

It should be noted that there is a large amount of redundant information acquired in a z-spectrum, which can be used to improve the CNR of the CEST contrast maps as recently demonstrated by Terreno et al.(90). They created new maps based on integration of B_0 corrected z-spectra to improve their quality. In this study, they tested a variety of data processing based on z-spectra including determining the areas under the spectrum around the CEST peak (A_{INT_PEAK}) or its complimentary (above the spectrum, $1-A_{INT\_PEAK}$), determining the areas under the spectrum from the CEST peak to water resonance (A_{INT_BULK}) or its complimentary (above the spectrum, $1-A_{INT\_BULK}$). In addition a new approach, a so-called enhanced mode, was used to define MTR^{ENC} with $[S(-\Delta\omega)-S(+\Delta\omega)]/S(-\Delta\omega)$, which is inversion version of MTR_{asym} defined by Eq. [11] with a relation of $MTR^{ENC}= 1/ MTR_{asym} -1$. It was indicated by the authors that the enhanced mode is more suitable for high CEST contrast, i.e. CEST effect >30%. While all the approaches using an integrated area have been shown to improve the CNR, the approach using area under spectrum (INT_PEAK) was shown to perform better for PARACEST agents with distant CEST peaks, and that using the areas above the spectrum (complimentary) may be better for DIACEST agents with small CEST effect and close to water resonance. In another recent study(38), this type of approach has been used to improve the detection of glycogen, where a cumulative CEST effect was calculated by numerically integrating CEST effect from 0 to 3 ppm.

Voxels with low SNR can compromise the accuracy of data interpolation, which has to be considered during data processing. There are several imaging process methods that have been reported to address this problem. For instance, we have been using *a priori* determined SNR maps to calculate CNR maps and filter out pixels with low CNR (3,91,108), based on the assumption that low CNR is due to either low SNR or low contrast. The advantage of using a CNR filter is that not only noisy pixels are filtered out but also those containing a low 'background' CEST contrast, allowing the filtered maps to highlight pixels possessing more reliable CEST contrast. However, the CNR threshold needs to be determined manually which may result in a bias. Another method which has been employed is a so-called median filter method(3), which is effective to remove 'salt and pepper' noise and can reduce the variations raised from interpolation. Very recently, a R^2 (the square of the correlation coefficient) filter was also introduced(149). In this approach, the R^2 for the interpolation curve with respect to the raw data was calculated pixel-wisely. Pixels with low R^2, i.e. <0.99, were discarded, assuming noisy z-spectra produce low R^2 values.

Frequency selective detection—One unique feature of CEST agents is that CEST contrast only occurs upon application of saturation pulses at particular frequencies (the characteristic frequencies of the CEST agents of interest). As a result, CEST allows detecting multiple agents simultaneously by their CEST offsets. This feature is very similar

to that of fluorescence dyes, inspiring the terminology of multi-color detection(3-5,122). The term frequency dependence encoded detection has also been used(6). Regardless of which term is used, multiple CEST agents can be detected simultaneously and displayed collectively as artificial color contrast maps. A CEST color spectrum (Fig. 11a) that is generated by encoding the DIACEST saturation offset with a color spectrum (4,5) and has been demonstrated in vivo (Fig. 11b)(3), provides guidelines for processing and displaying multiple DIACEST agents in future studies. The potential pitfalls of this approach is that, if the chemical shifts of two agents are not well separated, the detection of mixed type contrast within the same voxel can be challenging. PARACEST agents also have the capability of simultaneously detecting multiple agents (122,134). Because the chemical shifts of PARACEST agents are typically much more separated than those of DIACEST agents, the multi-color strategy of multiple PARACEST agents is therefore easier to be implemented and may have broader applications in the near future

The capability of simultaneously detecting multiple agents endows CEST contrast agents with clear advantages. For example, despite contrast agents being designed for a particular molecular biomarker, the apparent MRI contrast is influenced by a number of molecular environmental conditions and possibly by other molecular biomarkers. A solution to this problem is to apply a second contrast agent that is responsive to other molecular biomarkers/molecular environmental conditions or is unresponsive, serving as a “internal control”(121). This principle has been demonstrated using a pH responsive agent Yb-DOTAM-Gly together with a pH unresponsive agent Eu-DOTAM-Gly for pH measurement (17), with the pH determined by the ratio of two CEST contrasts from agents A and B:

$$\frac{\left(\frac{S_0}{S_S}-1\right)_A}{\left(\frac{S_0}{S_S}-1\right)_B}=\frac{[CA]_A\cdot n_A\cdot T_{1sat}}{[CA]_B\cdot n_B\cdot T_{1sat}}\cdot\frac{k_{SW}^A(pH)}{k_{SW}^B}=k\cdot\frac{k_{SW}^A(pH)}{k_{SW}^B} \quad [17]$$

in which only k_{SW}^A changes with pH, making the measurement independently from T1 and concentration of contrast agents since they share the same pharmacokinetics and hence have a constant concentration ratio.

Using molecules carrying multiple exchanging sites would further simplify the measurement:

$$\frac{\left(\frac{S_0}{S_S}-1\right)_{A1}}{\left(\frac{S_0}{S_S}-1\right)_{A2}}=\frac{[CA]_A\cdot n_{A1}\cdot T_{1sat}}{[CA]_A\cdot n_{A2}\cdot T_{1sat}}\cdot\frac{k_{SW}^{A1}}{k_{SW}^{A2}}=k\cdot\frac{k_{SW}^{A1}}{k_{SW}^{A2}} \quad [18]$$

where CEST agent A has two types exchangeable protons: A1 and A2. As long as their responsibilities to a particular biomarker is significantly different and their CEST effects are distinguishable, the ratio of their CEST effects could be used without the need to determine concentration(30). Based on this strategy, several CEST agents that contain two types of exchangeable protons have been developed for concentration independently measuring of pH (149,150), and are also possible to apply for measuring enzyme activity(41). It should be noted that the accuracy of these measurements highly depend on calibration curves. When

applied *in vivo*, MTC can complicate the measurements as MTC will also change as a function of frequency. It is expected that a technology well established to separate MTC and CEST contrast can greatly improve the *in vivo* applicability of the ratiometric approach.

Combining with other types of contrast maps to improve CEST contrast maps—One of the advantages of using CEST probes over T1 and T2* agents is that endogenous contrast can be retained. This unique feature endows the CEST MRI with the capability of using other MRI contrast for image segmentation and pixel classification to improve CEST quantification. For example, we have proposed an conventional MTC based segmentation technique for selectively filtering CEST contrast maps based on using the signal at two resonance frequency offsets $\Delta\omega_1$ and $\Delta\omega_2$ to calculate the NOrmalized MAgnetization Ratio (NOMAR)(151), defined by:

$$NOMAR(\Delta\omega_1/\Delta\omega_2) = (1 - MTR(\Delta\omega_1)) / (1 - MTR(\Delta\omega_2)) \quad [19]$$

MTC was chosen for its capability in classifying tissues (10) including separation of CSF containing pixels from brain parenchyma in MS studies (152) and removal of background tissue from contrast enhanced blood signal (153). When two additional MT weighted images are acquired at saturation frequencies of -12.5 ppm and -50 ppm, the NOMAR values, as calculated using Eq. [19], allow differentiation of voxels with low MT contrast (such as fat, CSF, edema or blood) from target tissue voxels using a global threshold determined by histogram analysis. Segmentation techniques based on other type of MRI contrast can also be used to create tissue selective CEST contrast maps, avoiding the potential complications caused by tissue saturation transfer properties.

SUMMARY

CEST imaging appears to be a very promising imaging technology for pre-clinical research and clinical diagnoses and prognoses. The technical hurdles for implementing CEST imaging in the clinic are being overcome through steady development of probes, hardware, and imaging schemes over the last decade, which have been summarized in the present work. With the aid of these technical advances, CEST imaging is now being tested in patients and has already shown utility in brain tumor diagnosis. It is hoped that the information in this review can assist other investigators interested in joining this promising field.

Acknowledgments

NIH grant support R01 EB015031, R01EB012590, R21EB015609.

Reference

1. Ward KM, Aletras AH, Balaban RS. A new class of contrast agents for MRI based on proton chemical exchange dependent saturation transfer (CEST). J Magn Reson. 2000; 143(1):79–87. [PubMed: 10698648]
2. Forsén S, Hoffman RA. Study of moderately rapid chemical exchange reactions by means of nuclear magnetic double resonance. The Journal of Chemical Physics. 1963; 39:2892.

3. Liu G, Moake M, Har-el YE, Long CM, Chan KW, Cardona A, Jamil M, Walczak P, Gilad AA, Sgouros G, van Zijl PC, Bulte JW, McMahon MT. In vivo multicolor molecular MR imaging using diamagnetic chemical exchange saturation transfer liposomes. Magn Reson Med. 2012; 67(4):1106–1113. [PubMed: 22392814]
4. Liu G, Gilad AA, Bulte JW, van Zijl PC, McMahon MT. High-throughput screening of chemical exchange saturation transfer MR contrast agents. Contrast Media Mol Imaging. 2010; 5(3):162–170. [PubMed: 20586030]
5. McMahon MT, Gilad AA, DeLiso MA, Cromer Berman SM, Bulte JWM, van Zijl PCM. New “multicolor” polypeptide diamagnetic chemical exchange saturation transfer (DIACEST) contrast agents for MRI. Magn Reson Med. 2008; 60(4):803–812. [PubMed: 18816830]
6. Terreno E, Castelli DD, Aime S. Encoding the frequency dependence in MRI contrast media: the emerging class of CEST agents. Contrast Media Mol Imaging. 2010; 5(2):78–98. [PubMed: 20419761]
7. Viswanathan S, Ratnakar SJ, Green KN, Kovacs Z, De Leon-Rodriguez LM, Sherry AD. Multi-frequency PARACEST agents based on europium(III)-DOTA-tetraamide ligands. Angew Chem. 2009; 48(49):9330–9333. [PubMed: 19894248]
8. Norris DG. High field human imaging. J Magn Reson Imaging. 2003; 18(5):519–529. [PubMed: 14579394]
9. Wolff SD, Balaban RS. Magnetization transfer contrast (MTC) and tissue water proton relaxation in vivo. Magn Reson Med. 1989; 10(1):135–144. [PubMed: 2547135]
10. Henkelman R, Stanisz G, Graham S. Magnetization transfer in MRI: a review. NMR Biomed. 2001; 14(2):57–64. [PubMed: 11320533]
11. van Zijl PC, Zhou J, Mori N, Payen JF, Wilson D, Mori S. Mechanism of magnetization transfer during on-resonance water saturation. A new approach to detect mobile proteins, peptides, and lipids. Magn Reson Med. 2003; 49(3):440–449. [PubMed: 12594746]
12. Kingsley PB, Monahan WG. Effects of off-resonance irradiation, cross-relaxation, and chemical exchange on steady-state magnetization and effective spin-lattice relaxation times. J Magn Reson. 2000; 143(2):360–375. [PubMed: 10729261]
13. Henkelman RM, Huang X, Xiang QS, Stanisz GJ, Swanson SD, Bronskill MJ. Quantitative interpretation of magnetization transfer. Magn Reson Med. 1993; 29(6):759–766. [PubMed: 8350718]
14. Morrison C, Stanisz G, Henkelman RM. Modeling magnetization transfer for biological-like systems using a semi-solid pool with a super-Lorentzian lineshape and dipolar reservoir. J Magn Reson B. 1995; 108(2):103–113. [PubMed: 7648009]
15. Zhou J, Wilson DA, Sun PZ, Klaus JA, Van Zijl PC. Quantitative description of proton exchange processes between water and endogenous and exogenous agents for WEX, CEST, and APT experiments. Magn Reson Med. 2004; 51(5):945–952. [PubMed: 15122676]
16. Goffeney N, Bulte JW, Duyn J, Bryant LH Jr. van Zijl PC. Sensitive NMR detection of cationic-polymer-based gene delivery systems using saturation transfer via proton exchange. JACS. 2001; 123(35):8628–8629.
17. Aime S, Barge A, Delli Castelli D, Fedeli F, Mortillaro A, Nielsen FU, Terreno E. Paramagnetic Lanthanide(III) complexes as pH-sensitive chemical exchange saturation transfer (CEST) contrast agents for MRI applications. Magn Reson Med. 2002; 47(4):639–648. [PubMed: 11948724]
18. Zhang S, Winter P, Wu K, Sherry AD. A novel europium(III)-based MRI contrast agent. JACS. 2001; 123(7):1517–1518.
19. Winter PM, Cai K, Chen J, Adair CR, Kiefer GE, Athey PS, Gaffney PJ, Buff CE, Robertson JD, Caruthers SD, Wickline SA, Lanza GM. Targeted PARACEST nanoparticle contrast agent for the detection of fibrin. Magn Reson Med. 2006; 56(6):1384–1388. [PubMed: 17089356]
20. Terreno E, Sanino A, Carrera C, Castelli DD, Giovenzana GB, Lombardi A, Mazzon R, Milone L, Visigalli M, Aime S. Determination of water permeability of paramagnetic liposomes of interest in MRI field. J Inorg Biochem. 2008; 102(5-6):1112–1119. [PubMed: 18329102]
21. Aime S, Delli Castelli D, Terreno E. Highly Sensitive MRI Chemical Exchange Saturation Transfer Agents Using Liposomes. Angew Chem. 2005; 117(34):5649–5651.

22. Zhao JM, Har-el YE, McMahon MT, Zhou J, Sherry AD, Sgouros G, Bulte JW, van Zijl PC. Size-induced enhancement of chemical exchange saturation transfer (CEST) contrast in liposomes. JACS. 2008; 130:5178–5184.
23. Flament J, Geffroy F, Medina C, Robic C, Mayer JF, Meriaux S, Valette J, Robert P, Port M, Le Bihan D, Lethimonnier F, Boumezbeur F. In vivo CEST MR imaging of U87 mice brain tumor angiogenesis using targeted LipoCEST contrast agent at 7 T. Magn Reson Med. 2012 doi:10.1002/mrm.24217.
24. Veshtort M, Griffin RG. SPINEVOLUTION: a powerful tool for the simulation of solid and liquid state NMR experiments. J Magn Reson. 2006; 178(2):248–282. [PubMed: 16338152]
25. Swanson S. Protein mediated magnetic coupling between lactate and water protons. J Magn Reson. 1998; 135(1):248–255. [PubMed: 9799702]
26. Estilaei M, Matson G, Meyerhoff D. Indirect imaging of ethanol via magnetization transfer at high and low magnetic fields. Magn Reson Med. 2003; 49(4):755–759. [PubMed: 12652547]
27. Schroder L, Lowery TJ, Hilty C, Wemmer DE, Pines A. Molecular imaging using a targeted magnetic resonance hyperpolarized biosensor. Science. 2006; 314(5798):446–449. [PubMed: 17053143]
28. Meldrum T, Seim KL, Bajaj VS, Palaniappan KK, Wu W, Francis MB, Wemmer DE, Pines A. A xenon-based molecular sensor assembled on an MS2 viral capsid scaffold. JACS. 2010; 132(17):5936–5937.
29. Taratula O, Hill PA, Bai Y, Khan NS, Dmochowski IJ. Shorter synthesis of trifunctionalized cryptophane-A derivatives. Org Lett. 2011; 13(6):1414–1417. [PubMed: 21332141]
30. Ward KM, Balaban RS. Determination of pH using water protons and chemical exchange dependent saturation transfer (CEST). Magn Reson Med. 2000; 44(5):799–802. [PubMed: 11064415]
31. Berger A, Loewenstein A, Meiboom S. Nuclear Magnetic Resonance Study of the Protolysis and Ionization of N-Methylacetamide1. JACS. 1959; 81(1):62–67.
32. Eigen M. Proton Transfer, Acid-Base Catalysis, and Enzymatic Hydrolysis. Part I: ELEMENTARY PROCESSES. Angewandte Chemie International Edition in English. 1964; 3(1):1–19.
33. Bai Y, Milne JS, Mayne L, Englander SW. Primary Structure Effects on Peptide Group Hydrogen Exchange. Proteins. 1993; 17:75–86. [PubMed: 8234246]
34. Hvidt A, Nielsen SO. Hydrogen exchange in proteins. Adv Protein Chem. 1966; 21:287–386. [PubMed: 5333290]
35. Esqueda AC, Lopez JA, Andreu-de-Riquer G, Alvarado-Monzon JC, Ratnakar J, Lubag AJ, Sherry AD, De Leon-Rodriguez LM. A new gadolinium-based MRI zinc sensor. JACS. 2009; 131(32):11387–11391.
36. Lubag AJ, De Leon-Rodriguez LM, Burgess SC, Sherry AD. Noninvasive MRI of beta-cell function using a Zn2+-responsive contrast agent. Proc Natl Acad Sci U S A. 2011; 108(45):18400–18405. [PubMed: 22025712]
37. Angelovski G, Chauvin T, Pohmann R, Logothetis NK, Toth E. Calcium-responsive paramagnetic CEST agents. Bioorg Med Chem. 2011; 19(3):1097–1105. [PubMed: 20691598]
38. Shah T, Lu L, Dell KM, Pagel MD, Griswold MA, Flask CA. CEST-FISP: a novel technique for rapid chemical exchange saturation transfer MRI at 7 T. Magn Reson Med. 2011; 65(2):432–437. [PubMed: 20939092]
39. Chan KWY, McMahon MT, Kato Y, Liu G, Bulte JWM, Bhujwalla ZM, Artemov D, van Zijl PCM. Natural D-glucose as a biodegradable MRI contrast agent for detecting cancer. Magn Reson Med. 2012 doi:10.1002/mrm.24520:n/a-n/a.
40. van Zijl PC, Jones CK, Ren J, Malloy CR, Sherry AD. MRI detection of glycogen in vivo by using chemical exchange saturation transfer imaging (glycoCEST). Proc Natl Acad Sci U S A. 2007; 104(11):4359–4364. [PubMed: 17360529]
41. Li Y, Sheth VR, Liu G, Pagel MD. A self-calibrating PARACEST MRI contrast agent that detects esterase enzyme activity. Contrast Media Mol Imaging. 2011; 6(4):219–228. [PubMed: 21861282]

42. Yoo B, Raam MS, Rosenblum RM, Pagel MD. Enzyme-responsive PARACEST MRI contrast agents: a new biomedical imaging approach for studies of the proteasome. Contrast Media Mol Imaging. 2007; 2(4):189–198. [PubMed: 17712869]
43. Yoo B, Pagel MD. A PARACEST MRI contrast agent to detect enzyme activity. JACS. 2006; 128(43):14032–14033.
44. Liu G, Liang Y, Bar-Shir A, Chan KW, Galpoththawela CS, Bernard SM, Tse T, Yadav NN, Walczak P, McMahon MT, Bulte JW, van Zijl PC, Gilad AA. Monitoring enzyme activity using a diamagnetic chemical exchange saturation transfer magnetic resonance imaging contrast agent. JACS. 2011; 133(41):16326–16329.
45. Cai K, Haris M, Singh A, Kogan F, Greenberg JH, Hariharan H, Detre JA, Reddy R. Magnetic resonance imaging of glutamate. Nat Med. 2012; 18(2):302–306. [PubMed: 22270722]
46. Haris M, Cai K, Singh A, Hariharan H, Reddy R. In vivo mapping of brain myo inositol. Neuroimage. 2011; 54(3):2079–2085. [PubMed: 20951217]
47. Aime S, Delli Castelli D, Fedeli F, Terreno E. A paramagnetic MRI-CEST agent responsive to lactate concentration. JACS. 2002; 124(32):9364–9365.
48. Ratnakar SJ, Viswanathan S, Kovacs Z, Jindal AK, Green KN, Sherry AD. Europium(III) DOTA-tetraamide complexes as redox-active MRI sensors. JACS. 2012; 134(13):5798–5800.
49. De Leon-Rodriguez LM, Lubag AJ, Malloy CR, Martinez GV, Gillies RJ, Sherry AD. Responsive MRI agents for sensing metabolism in vivo. Acc Chem Res. 2009; 42(7):948–957. [PubMed: 19265438]
50. Liu G, Li Y, Pagel MD. Design and characterization of a new irreversible responsive PARACEST MRI contrast agent that detects nitric oxide. Magn Reson Med. 2007; 58(6):1249–1256. [PubMed: 18046705]
51. Zhou J, Payen JF, Wilson DA, Traystman RJ, van Zijl PCM. Using the amide proton signals of intracellular proteins and peptides to detect pH effects in MRI. Nat Med. 2003; 9(8):1085–1090. [PubMed: 12872167]
52. Zhou J, Lal B, Wilson DA, Laterra J, van Zijl PCM. Amide proton transfer (APT) contrast for imaging of brain tumors. Magn Reson Med. 2003; 50(6):1120–1126. [PubMed: 14648559]
53. Zhou J, Tryggestad E, Wen Z, Lal B, Zhou T, Grossman R, Wang S, Yan K, Fu DX, Ford E, Tyler B, Blakeley J, Laterra J, van Zijl PC. Differentiation between glioma and radiation necrosis using molecular magnetic resonance imaging of endogenous proteins and peptides. Nat Med. 2011; 17(1):130–134. [PubMed: 21170048]
54. Delli Castelli D, Terreno E, Aime S. Yb(III)-HPDO3A: a dual pH- and temperature-responsive CEST agent. Angew Chem Int Ed Engl. 2011; 50(8):1798–1800. [PubMed: 21328642]
55. Zhang S, Malloy CR, Sherry AD. MRI thermometry based on PARACEST agents. JACS. 2005; 127(50):17572–17573.
56. Schilling F, Schroder L, Palaniappan KK, Zapf S, Wemmer DE, Pines A. MRI thermometry based on encapsulated hyperpolarized xenon. Chemphyschem : a European journal of chemical physics and physical chemistry. 2010; 11(16):3529–3533. [PubMed: 20821795]
57. Wen Z, Hu S, Huang F, Wang X, Guo L, Quan X, Wang S, Zhou J. MR imaging of high-grade brain tumors using endogenous protein and peptide-based contrast. Neuroimage. 2010; 51(2):616–622. [PubMed: 20188197]
58. Jia G, Abaza R, Williams JD, Zynger DL, Zhou J, Shah ZK, Patel M, Sammet S, Wei L, Bahnson RR, Knopp MV. Amide proton transfer MR imaging of prostate cancer: a preliminary study. J Magn Reson Imaging. 2011; 33(3):647–654. [PubMed: 21563248]
59. Sun PZ, Wang E, Cheung JS. Imaging acute ischemic tissue acidosis with pH-sensitive endogenous amide proton transfer (APT) MRI-Correction of tissue relaxation and concomitant RF irradiation effects toward mapping quantitative cerebral tissue pH. Neuroimage. 2012; 60(1):1–6. [PubMed: 22178815]
60. Delli Castelli D, Dastru W, Terreno E, Cittadino E, Mainini F, Torres E, Spadaro M, Aime S. In vivo MRI multicontrast kinetic analysis of the uptake and intracellular trafficking of paramagnetically labeled liposomes. J Controlled Release. 2010; 144(3):271–279.

61. Choi J, Kim K, Kim T, Liu G, Bar-Shir A, Hyeon T, McMahon MT, Bulte JW, Fisher JP, Gilad AA. Multimodal imaging of sustained drug release from 3-D poly(propylene fumarate) (PPF) scaffolds. J Control Release. 2011; 156(2):239–245. [PubMed: 21763735]
62. Varma G, Lenkinski RE, Vinogradov E. Keyhole chemical exchange saturation transfer. Magn Reson Med. 2012; 68(4):1228–1233. [PubMed: 22246655]
63. Krusche-Mandl I, Schmitt B, Zak L, Apprich S, Aldrian S, Juras V, Friedrich KM, Marlovits S, Weber M, Trattnig S. Long-term results 8 years after autologous osteochondral transplantation: 7 T gagCEST and sodium magnetic resonance imaging with morphological and clinical correlation. Osteoarthritis Cartilage. 2012 doi:10.1016/j.joca.2012.01.020.
64. Ling W, Regatte RR, Navon G, Jerschow A. Assessment of glycosaminoglycan concentration in vivo by chemical exchange-dependent saturation transfer (gagCEST). Proc Natl Acad Sci U S A. 2008; 105(7):2266–2270. [PubMed: 18268341]
65. Gilad AA, McMahon MT, Walczak P, Winnard PT Jr. Raman V, van Laarhoven HW, Skoglund CM, Bulte JW, van Zijl PC. Artificial reporter gene providing MRI contrast based on proton exchange. Nat Biotechnol. 2007; 25(2):217–219. [PubMed: 17259977]
66. Aime S, Castelli DD, Crich SG, Gianolio E, Terreno E. Pushing the sensitivity envelope of lanthanide-based magnetic resonance imaging (MRI) contrast agents for molecular imaging applications. Acc Chem Res. 2009; 42(7):822–831. [PubMed: 19534516]
67. Zhang S, Merritt M, Woessner DE, Lenkinski RE, Sherry AD. PARACEST agents: modulating MRI contrast via water proton exchange. Acc Chem Res. 2003; 36(10):783–790. [PubMed: 14567712]
68. Woods M, Woessner DE, Sherry AD. Paramagnetic lanthanide complexes as PARACEST agents for medical imaging. Chem Soc Rev. 2006; 35(6):500–511. [PubMed: 16729144]
69. Hancu I, Dixon WT, Woods M, Vinogradov E, Sherry AD, Lenkinski RE. CEST and PARACEST MR contrast agents. Acta Radiol. 2010; 51(8):910–923. [PubMed: 20828299]
70. Sherry AD, Woods M. Chemical exchange saturation transfer contrast agents for magnetic resonance imaging. Annu Rev Biomed Eng. 2008; 10:391–411. [PubMed: 18647117]
71. Zhou J, van Zijl PCM. Chemical exchange saturation transfer imaging and spectroscopy. Prog Nucl Magn Reson Spectrosc. 2006; 48(2-3):109–136.
72. van Zijl PC, Yadav NN. Chemical exchange saturation transfer (CEST): what is in a name and what isn't? Magn Reson Med. 2011; 65(4):927–948. [PubMed: 21337419]
73. Friedman JI, McMahon MT, Stivers JT, Van Zijl PCM. Indirect Detection of Labile Solute Proton Spectra via the Water Signal Using Frequency-Labeled Exchange (FLEX) Transfer. JACS. 2010; 132(6):1813–1815.
74. Vinogradov E, Soesbe TC, Balschi JA, Sherry AD, Lenkinski RE. pCEST: Positive contrast using Chemical Exchange Saturation Transfer. J Magn Reson. 2012; 215:64–73. [PubMed: 22237630]
75. Jin T, Wang P, Zong XP, Kim SG. Magnetic resonance imaging of the Amine-Proton EXchange (APEX) dependent contrast. Neuroimage. 2012; 59(2):1218–1227. [PubMed: 21871570]
76. Cobb JG, Xie JP, Li K, Gochberg DF, Gore JC. Exchange-mediated contrast agents for spin-lock imaging. Magn Reson Med. 2012; 67(5):1427–1433. [PubMed: 21954094]
77. Garcia S, Chavez L, Lowery TJ, Han SI, Wemmer DE, Pines A. Sensitivity enhancement by exchange mediated magnetization transfer of the xenon biosensor signal. J Magn Reson. 2007; 184(1):72–77. [PubMed: 17046295]
78. McMahon MT, Gilad AA, Zhou J, Sun PZ, Bulte JWM, van Zijl PCM. Quantifying exchange rates in chemical exchange saturation transfer agents using the saturation time and saturation power dependencies of the magnetization transfer effect on the magnetic resonance imaging signal (QUEST and QUESP): Ph calibration for poly-L-lysine and a starburst dendrimer. Magn Reson Med. 2006; 55(4):836–847. [PubMed: 16506187]
79. Woessner DE, Zhang S, Merritt ME, Sherry AD. Numerical solution of the Bloch equations provides insights into the optimum design of PARACEST agents for MRI. Magn Reson Med. 2005; 53(4):790–799. [PubMed: 15799055]
80. Sun PZ, Zhou J, Huang J, van Zijl P. Simplified quantitative description of amide proton transfer (APT) imaging during acute ischemia. Magn Reson Med. 2007; 57(2):405–410. [PubMed: 17260362]

81. Sun PZ, van Zijl PC, Zhou J. Optimization of the irradiation power in chemical exchange dependent saturation transfer experiments. J Magn Reson. 2005; 175(2):193–200. [PubMed: 15893487]
82. Sun PZ. Simplified and scalable numerical solution for describing multi-pool chemical exchange saturation transfer (CEST) MRI contrast. J Magn Reson. 2010; 205(2):235–241. [PubMed: 20570196]
83. Desmond KL, Stanisz GJ. Understanding quantitative pulsed CEST in the presence of MT. Magn Reson Med. 2011 doi:10.1002/mrm.23074.
84. Zu Z, Li K, Janve VA, Does MD, Gochberg DF. Optimizing pulsed-chemical exchange saturation transfer imaging sequences. Magn Reson Med. 2011; 66(4):1100–1108. [PubMed: 21432903]
85. Li A, Hudson R, Barrett J, Jones C, Pasternak S, Bartha R. Four-pool modeling of proton exchange processes in biological systems in the presence of MRI–paramagnetic chemical exchange saturation transfer (PARACEST) agents. Magn Reson Med. 2008; 60(5):1197–1206. [PubMed: 18958857]
86. Grad J, Bryant RG. Nuclear magnetic cross-relaxation spectroscopy. Journal of Magnetic Resonance (1969). 1990; 90(1):1–8.
87. Guivel-Scharen V, Sinnwell T, Wolff SD, Balaban RS. Detection of proton chemical exchange between metabolites and water in biological tissues. J Magn Reson. 1998; 133(1):36–45. [PubMed: 9654466]
88. Hua J, Jones CK, Blakeley J, Smith SA, van Zijl PC, Zhou J. Quantitative description of the asymmetry in magnetization transfer effects around the water resonance in the human brain. Magn Reson Med. 2007; 58(4):786–793. [PubMed: 17899597]
89. Sun PZ, Zhou J, Sun W, Huang J, van Zijl PCM. Detection of the ischemic penumbra using pH-weighted MRI. J Cereb Blood Flow Metab. 2006; 27(6):1129–1136. [PubMed: 17133226]
90. Terreno E, Stancanello J, Longo D, Castelli DD, Milone L, Sanders HMHF B, Kok M, Uggeri F, Aime S. Methods for an improved detection of the MRI-CEST effect. Contrast Media Mol Imaging. 2009; 4(5):237–247. [PubMed: 19839029]
91. Liu G, Ali MM, Yoo B, Griswold MA, Tkach JA, Pagel MD. PARACEST MRI with improved temporal resolution. Magn Reson Med. 2009; 61(2):399–408. [PubMed: 19165903]
92. Gutowsky HS, McCall DW, Slichter CP. Nuclear Magnetic Resonance Multiplets in Liquids. J Chem Phys. 1953; 21(2):279–292.
93. Gutowsky HS, Saika A. Dissociation, Chemical Exchange, and the Proton Magnetic Resonance in Some Aqueous Electrolytes. J Chem Phys. 1953; 21(10):1688–1694.
94. Mori S, Abeygunawardana C, Zijl Pv, Berg J. Water exchange filter with improved sensitivity (WEX II) to study solvent-exchangeable protons. application to the consensus zinc finger peptide CP-1. J Magn Reson B. 1996; 110:96–101. [PubMed: 8556240]
95. Mori S, Berg JM, van Zijl PCM. Separation of intramolecular NOE and exchange peaks in water exchange spectroscopy using spin-echo filters. J Biomol NMR. 1996; 7:77–82. [PubMed: 8720834]
96. Dixon WT, Ren J, Lubag AJ, Ratnakar J, Vinogradov E, Hancu I, Lenkinski RE, Sherry AD. A concentration-independent method to measure exchange rates in PARACEST agents. Magn Reson Med. 2010; 63(3):625–632. [PubMed: 20187174]
97. Sun PZ. Simplified quantification of labile proton concentration-weighted chemical exchange rate (k(ws)) with RF saturation time dependent ratiometric analysis (QUESTRA): normalization of relaxation and RF irradiation spillover effects for improved quantitative chemical exchange saturation transfer (CEST) MRI. Magn Reson Med. 2012; 67(4):936–942. [PubMed: 21842497]
98. Zu Z, Janve VA, Li K, Does MD, Gore JC, Gochberg DF. Multi-angle ratiometric approach to measure chemical exchange in amide proton transfer imaging. Magn Reson Med. 2011 doi: 10.1002/mrm.23276:n/a-n/a.
99. Zu Z, Janve VA, Li K, Does MD, Gore JC, Gochberg DF. Multi-angle ratiometric approach to measure chemical exchange in amide proton transfer imaging. Magn Reson Med. 2012; 68(3): 711–719. [PubMed: 22161770]
100. Lin CY, Yadav NN, Friedman JI, Ratnakar J, Sherry AD, van Zijl PCM. Using Frequency-Labeled Exchange Transfer to Separate Out Conventional Magnetization Transfer Effects From

Exchange Transfer Effects When Detecting ParaCEST Agents. Magn Reson Med. 2012; 67(4): 906–911. [PubMed: 22287162]

101. Uematsu H, Takahashi M, Dougherty L, Hatabu H. High field body MR imaging: preliminary experiences. Clin Imaging. 2004; 28(3):159–162. [PubMed: 15158217]
102. Sun PZ, Murata Y, Lu J, Wang X, Lo EH, Sorensen AG. Relaxation-compensated fast multislice amide proton transfer (APT) imaging of acute ischemic stroke. Magn Reson Med. 2008; 59(5): 1175–1182. [PubMed: 18429031]
103. Zhu H, Jones CK, van Zijl PCM, Barker PB, Zhou J. Fast 3D chemical exchange saturation transfer (CEST) imaging of the human brain. Magn Reson Med. 2010; 64(3):638–644. [PubMed: 20632402]
104. Zhang S, Zhu X, Chen Z, Cai C, Lin T, Zhong J. Improvement in the contrast of CEST MRI via intermolecular double quantum coherences. Phys Med Biol. 2008; 53(14):N287–296. [PubMed: 18574314]
105. Ling W, Eliav U, Navon G, Jerschow A. Chemical exchange saturation transfer by intermolecular double-quantum coherence. J Magn Reson. 2008; 194(1):29–32. [PubMed: 18571444]
106. Schneider E, Prost RW, Glover GH. Pulsed magnetization transfer versus continuous wave irradiation for tissue contrast enhancement. J Magn Reson Imaging. 1993; 3(2):417–423. [PubMed: 8448405]
107. Sun PZ, Sorensen AG. Imaging pH using the chemical exchange saturation transfer (CEST) MRI: Correction of concomitant RF irradiation effects to quantify CEST MRI for chemical exchange rate and pH. Magn Reson Med. 2008; 60(2):390–397. [PubMed: 18666128]
108. Liu, D.; Zhou, J.; Xue, R.; Zuo, Z.; An, J.; Wang, DJJ. RF Power Dependence of Human Brain CEST, NOE and Metabolite MT Effects at 7T. Melbourne, Australia: 2012.
109. Dmitrov, IE.; Takahashi, M.; Sagiyama, K.; Sherry, AD.; Keupp, J. In vivo human kidney pH mapping at 3T using time-interleaved parallel RF transmission CEST. Melbourne, Australia: 2012.
110. Meldrum T, Bajaj VS, Wemmer DE, Pines A. Band-selective chemical exchange saturation transfer imaging with hyperpolarized xenon-based molecular sensors. J Magn Reson. 2011; 213(1):14–21. [PubMed: 21974996]
111. Dixon WT, Hancu I, Ratnakar SJ, Sherry AD, Lenkinski RE, Alsop DC. A multislice gradient echo pulse sequence for CEST imaging. Magn Reson Med. 2010; 63(1):253–256. [PubMed: 19918889]
112. Aime S, Delli Castelli D, Terreno E. Novel pH-reporter MRI contrast agents. Angew Chem. 2002; 114(22):4510–4512.
113. Schmitt B, Zaiss M, Zhou J, Bachert P. Optimization of pulse train presaturation for CEST imaging in clinical scanners. Magn Reson Med. 2011; 65(6):1620–1629. [PubMed: 21337418]
114. Scheidegger R, Vinogradov E, Alsop DC. Amide proton transfer imaging with improved robustness to magnetic field inhomogeneity and magnetization transfer asymmetry using saturation with frequency alternating RF irradiation. Magn Reson Med. 2011; 66(5):1275–1285. [PubMed: 21608029]
115. Zabow G, Dodd SJ, Shapiro E, Moreland J, Koretsky AP. Microfabricated high-moment micrometer-sized MRI contrast agents. Magn Reson Med. 2011; 65(3):645–655. [PubMed: 20928829]
116. Sun PZ, Benner T, Kumar A, Sorensen AG. Investigation of optimizing and translating pH-sensitive pulsed-chemical exchange saturation transfer (CEST) imaging to a 3T clinical scanner. Magn Reson Med. 2008; 60(4):834–841. [PubMed: 18816867]
117. Narvainen J, Hubbard PL, Kauppinen RA, Morris GA. Z-spectroscopy with Alternating-Phase Irradiation. J Magn Reson. 2010; 207(2):242–250. [PubMed: 20920868]
118. Lee JS, Regatte RR, Jerschow A. Isolating chemical exchange saturation transfer contrast from magnetization transfer asymmetry under two-frequency rf irradiation. J Magn Reson. 2012; 215:56–63. [PubMed: 22237631]
119. Vinogradov E, Zhang S, Lubag A, Balschi J, Sherry A, Lenkinski R. On-resonance low pulses for imaging of the effects of PARACEST agents. J Magn Reson. 2005; 176(1):54–63. [PubMed: 15979362]

120. Zabow G, Dodd SJ, Moreland J, Koretsky AP. The fabrication of uniform cylindrical nanoshells and their use as spectrally tunable MRI contrast agents. Nanotechnology. 2009; 20(38):385301. [PubMed: 19713581]
121. Ali MM, Liu G, Shah T, Flask CA, Pagel MD. Using two chemical exchange saturation transfer magnetic resonance imaging contrast agents for molecular imaging studies. Acc Chem Res. 2009; 42(7):915–924. [PubMed: 19514717]
122. Aime S, Carrera C, Delli Castelli D, Geninatti Crich S, Terreno E. Tunable Imaging of Cells Labeled with MRI-PARACEST Agents. Angew Chem Int Ed. 2005; 44(12):1813–1815.
123. Zhou J, Blakeley JO, Hua J, Kim M, Laterra J, Pomper MG, van Zijl PC. Practical data acquisition method for human brain tumor amide proton transfer (APT) imaging. Magn Reson Med. 2008; 60(4):842–849. [PubMed: 18816868]
124. Vinogradov E, He H, Lubag A, Balschi JA, Sherry AD, Lenkinski RE. MRI detection of paramagnetic chemical exchange effects in mice kidneys in vivo. Magn Reson Med. 2007; 58(4): 650–655. [PubMed: 17899603]
125. Song X, Gilad AA, Joel S, Liu G, Bar-Shir A, Liang Y, Gorelik M, Pekar JJ, van Zijl PC, Bulte JW, McMahon MT. CEST phase mapping using a length and offset varied saturation (LOVARS) scheme. Magn Reson Med. 2012; 68(4):1074–1086. [PubMed: 22246684]
126. McGibney G, Smith MR, Nichols ST, Crawley A. Quantitative evaluation of several partial Fourier reconstruction algorithms used in MRI. Magn Reson Med. 1993; 30(1):51–59. [PubMed: 8371675]
127. Hu X, Parrish T. Reduction of field of view for dynamic imaging. Magn Reson Med. 1994; 31(6): 691–694. [PubMed: 8057824]
128. van Vaals JJ, Brummer ME, Dixon WT, Tuithof HH, Engels H, Nelson RC, Gerety BM, Chezmar JL, den Boer JA. “Keyhole” method for accelerating imaging of contrast agent uptake. J Magn Reson Imaging. 1993; 3(4):671–675. [PubMed: 8347963]
129. Lustig M, Donoho D, Pauly JM. Sparse MRI: The application of compressed sensing for rapid MR imaging. Magn Reson Med. 2007; 58(6):1182–1195. [PubMed: 17969013]
130. Sun PZ, Zhou J, Sun W, Huang J, van Zijl PCM. Suppression of lipid artifacts in amide proton transfer imaging. Magn Reson Med. 2005; 54(1):222–225. [PubMed: 15968669]
131. Jones CK, Polders D, Hua J, Zhu H, Hoogduin HJ, Zhou J, Luijten P, van Zijl PCM. In vivo three-dimensional whole-brain pulsed steady-state chemical exchange saturation transfer at 7 T. Magn Reson Med. 2011 doi:10.1002/mrm.23141:n/a-n/a.
132. Jones CK, Polders D, Hua J, Zhu H, Hoogduin HJ, Zhou J, Luijten P, van Zijl PC. In vivo three-dimensional whole-brain pulsed steady-state chemical exchange saturation transfer at 7 T. Magn Reson Med. 2012; 67(6):1579–1589. [PubMed: 22083645]
133. Sun PZ, Cheung JS, Wang E, Benner T, Sorensen AG. Fast multislice pH-weighted chemical exchange saturation transfer (CEST) MRI with Unevenly segmented RF irradiation. Magn Reson Med. 2011; 65(2):588–594. [PubMed: 20872859]
134. Lee JS, Khitrin AK, Regatte RR, Jerschow A. Uniform saturation of a strongly coupled spin system by two-frequency irradiation. The Journal of chemical physics. 2011; 134(23):234504. [PubMed: 21702564]
135. Yadav, NN.; Bar-Shir, A.; Jones, CK.; Lin, CY.; Hua, J.; Gilad, AA.; McMahon, MT.; van Zijl, PC. International Society of Magnetic Resonance in Medicine. Vol. 20. Melbourne, Australia: 2012. Exchange rate filtering of CEST agents using frequency-labeled exchange (FLEX) transfer.; p. 4189
136. Song, X.; Chan, K.; Liu, G.; Arifin, D.; Gilad, A.; van Zijl, P.; Bulte, J.; McMahon, M. Imaging of DIACEST Microcapsules containing Hepatocytes using Length VARiation of Saturation(LVARS) and Principle Component Analysis. Montreal, Canada: 2011. p. 1701
137. Friston KJ, Holmes AP, Worsley KJ, Poline JP, Frith CD, Frackowiak RSJ. Statistical parametric maps in functional imaging: a general linear approach. Hum Brain Mapp. 1994; 2(4):189–210.
138. Liu G, Gilad AA. MRI of CEST-based reporter gene. Methods Mol Biol. 2011; 771:733–746. [PubMed: 21874505]

139. Stancanello J, Terreno E, Castelli DD, Cabella C, Uggeri F, Aime S. Development and validation of a smoothing-splines-based correction method for improving the analysis of CEST-MR images. Contrast Media Mol Imaging. 2008; 3(4):136–149. [PubMed: 18683280]

140. Sun PZ, Farrar CT, Sorensen AG. Correction for artifacts induced by B0 and B1 field inhomogeneities in pH-sensitive chemical exchange saturation transfer (CEST) imaging. Magn Reson Med. 2007; 58(6):1207–1215. [PubMed: 17969015]

141. Duerk JL, Pattany PM. In-plane flow velocity quantification along the phase encoding axis in MRI. Magn Reson Imaging. 1988; 6(3):321–333. [PubMed: 3398740]

142. Hedley M, Rosenfeld D. A new two-dimensional phase unwrapping algorithm for MRI images. Magn Reson Med. 1992; 24(1):177–181. [PubMed: 1556925]

143. Kim M, Gillen J, Landman BA, Zhou J, van Zijl PC. Water saturation shift referencing (WASSR) for chemical exchange saturation transfer (CEST) experiments. Magn Reson Med. 2009; 61(6): 1441–1450. [PubMed: 19358232]

144. Mulkern RV, Williams ML. The general solution to the Bloch equation with constant rf and relaxation terms: application to saturation and slice selection. Med Phys. 1993; 20(1):5–13. [PubMed: 8455512]

145. Singh A, Cai K, Haris M, Hariharan H, Reddy R. On B(1) inhomogeneity correction of in vivo human brain glutamate chemical exchange saturation transfer contrast at 7T. Magn Reson Med. 2012 doi:10.1002/mrm.24290.

146. Morrison C, Henkelman RM. A model for magnetization transfer in tissues. Magn Reson Med. 1995; 33(4):475–482. [PubMed: 7776877]

147. Zaiß M, Schmitt B, Bachert P. Quantitative separation of CEST effect from magnetization transfer and spillover effects by Lorentzian-line-fit analysis of z-spectra. J Magn Reson. 2011; 211(2):149–155. [PubMed: 21641247]

148. Zaiss M, Schnurr M, Bachert P. Analytical solution for the depolarization of hyperpolarized nuclei by chemical exchange saturation transfer between free and encapsulated xenon (HyperCEST). The Journal of chemical physics. 2012; 136(14):144106. [PubMed: 22502500]

149. Longo DL, Dastru W, Digilio G, Keupp J, Langereis S, Lanzardo S, Prestigio S, Steinbach O, Terreno E, Uggeri F, Aime S. Iopamidol as a responsive MRI-chemical exchange saturation transfer contrast agent for pH mapping of kidneys: In vivo studies in mice at 7 T. Magn Reson Med. 2011; 65(1):202–211. [PubMed: 20949634]

150. Liu G, Li Y, Sheth VR, Pagel MD. Imaging In Vivo Extracellular pH with a Single Paramagnetic Chemical Exchange Saturation Transfer Magnetic Resonance Imaging Contrast Agent. Mol Imaging. 2011 doi:10.2310/7290.2011.00026.

151. Liu G, Chan KW, Song X, Zhang J, Gilad AA, Bulte JW, van Zijl PC, McMahon MT. Normalized magnetization ratio (NOMAR) filtering for creation of tissue selective contrast maps. Magn Reson Med. 2012 doi:10.1002/mrm.24271.

152. Kalkers NF, Hintzen RQ, van Waesberghe JH, Lazeron RH, van Schijndel RA, Ader HJ, Polman CH, Barkhof F. Magnetization transfer histogram parameters reflect all dimensions of MS pathology, including atrophy. J Neurol Sci. 2001; 184(2):155–162. [PubMed: 11239950]

153. Parker DL, Buswell HR, Goodrich KC, Alexander AL, Keck N, Tsuruda JS. The application of magnetization transfer to MR angiography with reduced total power. Magn Reson Med. 1995; 34(2):283–286. [PubMed: 7476089]

154. Makela HI, De Vita E, Grohn OH, Kettunen MI, Kavec M, Lythgoe M, Garwood M, Ordidge R, Kauppinen RA. B0 dependence of the on-resonance longitudinal relaxation time in the rotating frame (T1rho) in protein phantoms and rat brain in vivo. Magn Reson Med. 2004; 51(1):4–8. [PubMed: 14705038]

155. de Graaf RA, Brown PB, McIntyre S, Nixon TW, Behar KL, Rothman DL. High magnetic field water and metabolite proton T1 and T2 relaxation in rat brain in vivo. Magn Reson Med. 2006; 56(2):386–394. [PubMed: 16767752]

156. Pham M, Helluy X, Kleinschnitz C, Kraft P, Bartsch AJ, Jakob P, Nieswandt B, Bendszus M, Stoll G. Sustained reperfusion after blockade of glycoprotein-receptor-Ib in focal cerebral ischemia: an MRI study at 17.6 Tesla. PLoS ONE. 2011; 6(4):e18386. [PubMed: 21483769]

157. van de Ven RC, Hogers B, van den Maagdenberg AM, de Groot HJ, Ferrari MD, Frants RR, Poelmann RE, van der Weerd L, Kiihne SR. T(1) relaxation in in vivo mouse brain at ultra-high field. Magn Reson Med. 2007; 58(2):390–395. [PubMed: 17654587]

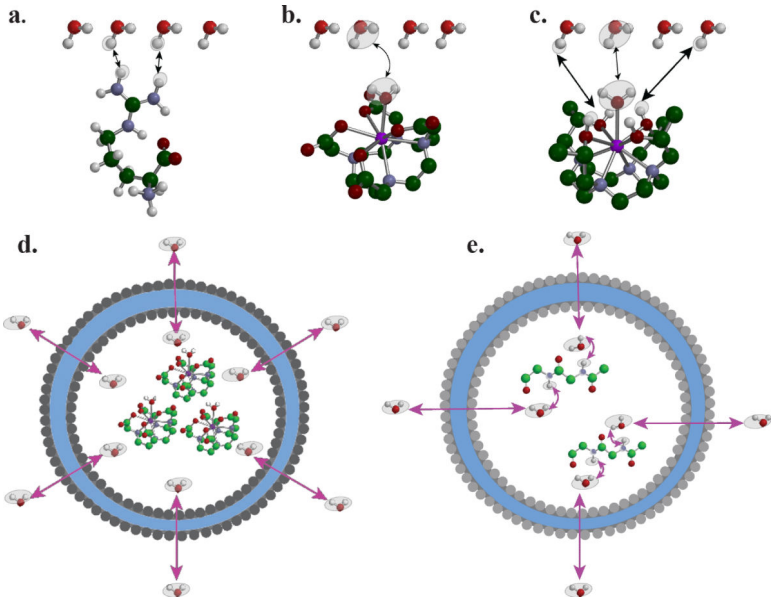

Figure 1.

The exchange pathways that can result in CEST contrast: **a)** proton exchange; **b**) molecule exchange; **c)** proton+molecule; **d)** compartment exchange; and **e)** macromolecule mediated compartment exchange.

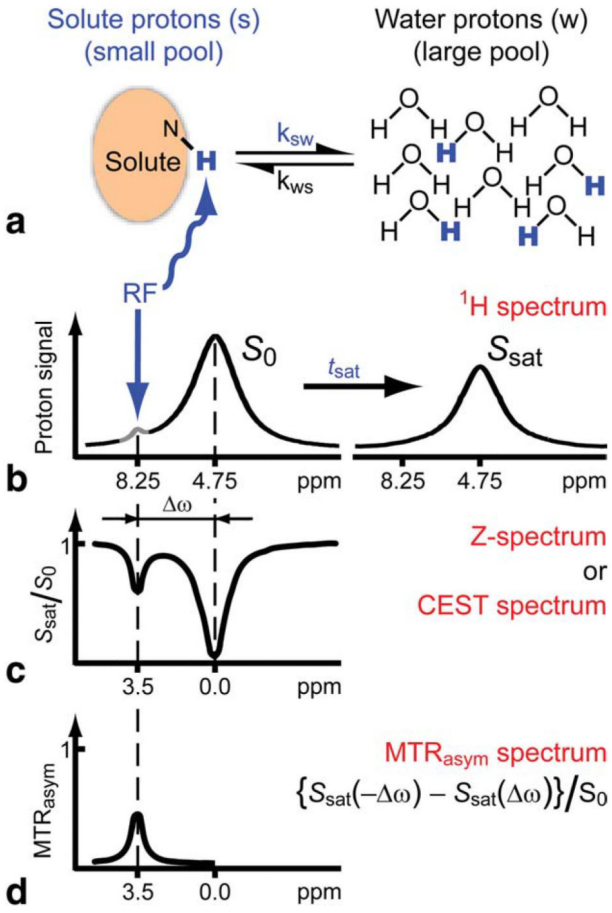

Figure 2.

Schematic of Chemical exchange saturation transfer (CEST): principles and measurement approach for pure exchange effects. **a, b)** Solute protons (blue) are saturated at their specific resonance frequency in the proton spectrum (here 8.25 ppm for amide protons). This saturation is transferred to water (4.75 ppm) at exchange rate k_{sw} and nonsaturated protons (black) return. After a period (t_{sat}), this effect becomes visible on the water signal (**b**, right). **c)** Measurement of normalized water saturation (Ssat/S0) as a function of irradiation frequency, generating a so-called z-spectrum (or CEST spectrum or MT spectrum). When irradiating the water protons at 4.75 ppm, the signal disappears due to direct (water) saturation (DS). This frequency is assigned to 0 ppm in z-spectra. At short saturation times, only this direct saturation is apparent. At longer t_{sat} the CEST effect becomes visible at the frequency of the low- concentration exchangeable solute protons, now assigned to 8.25 - 4.75 = 3.5 ppm in the z-spectrum. **d)** result of magnetization transfer ratio asymmetry analysis of the z-spectrum with respect to the water frequency to remove the effect of direct saturation. *Reproduced from reference (11) with permission.*

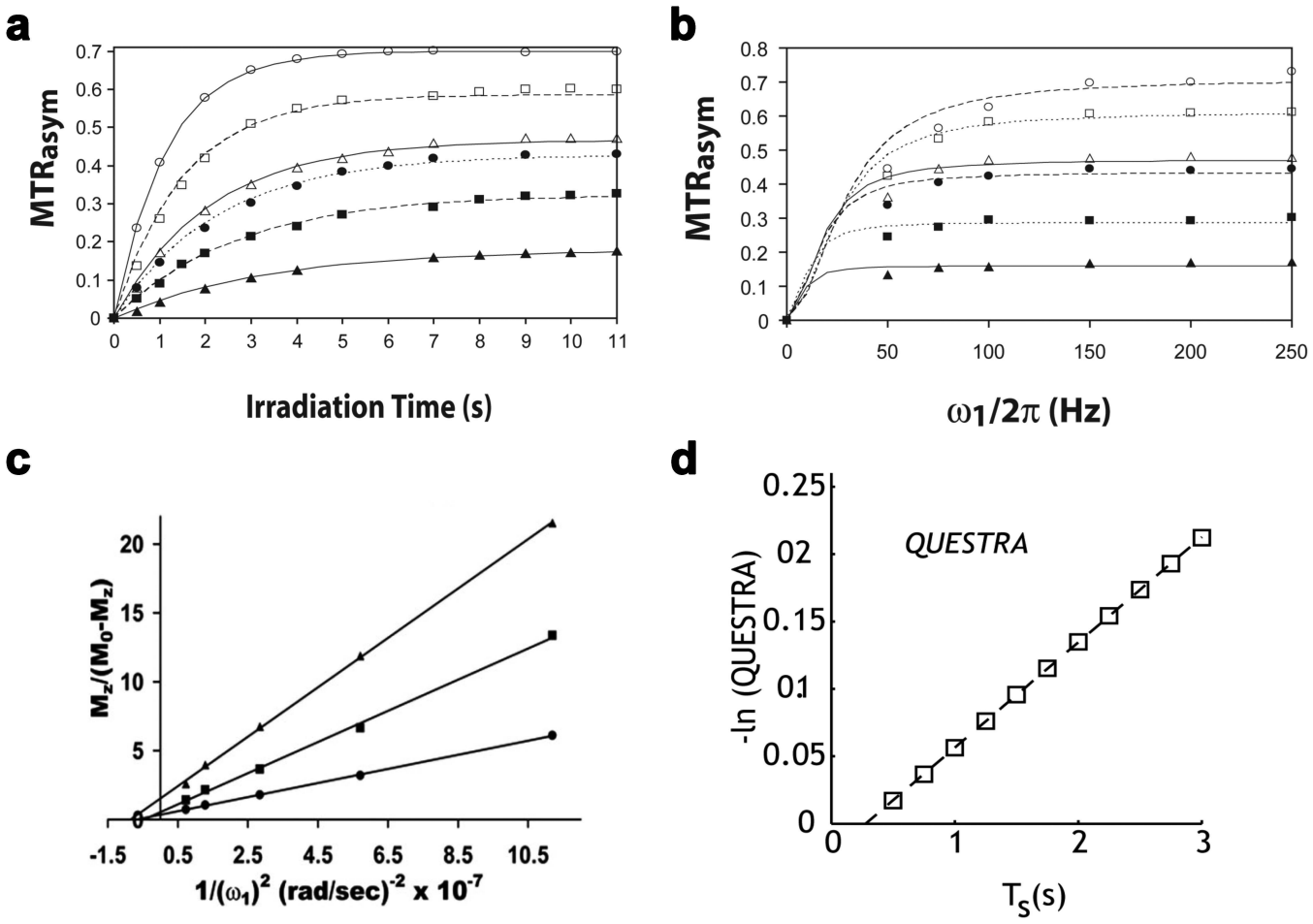

Figure 3.

Four MRI methods for estimating exchange using varied saturation power or saturation time. **a)** QUEST; **b)** QUESP; **c)** Omega plot; and **d)** QUESTRA. These were reproduced from reference(78) (a-b), (96) (c), and(97) (d).

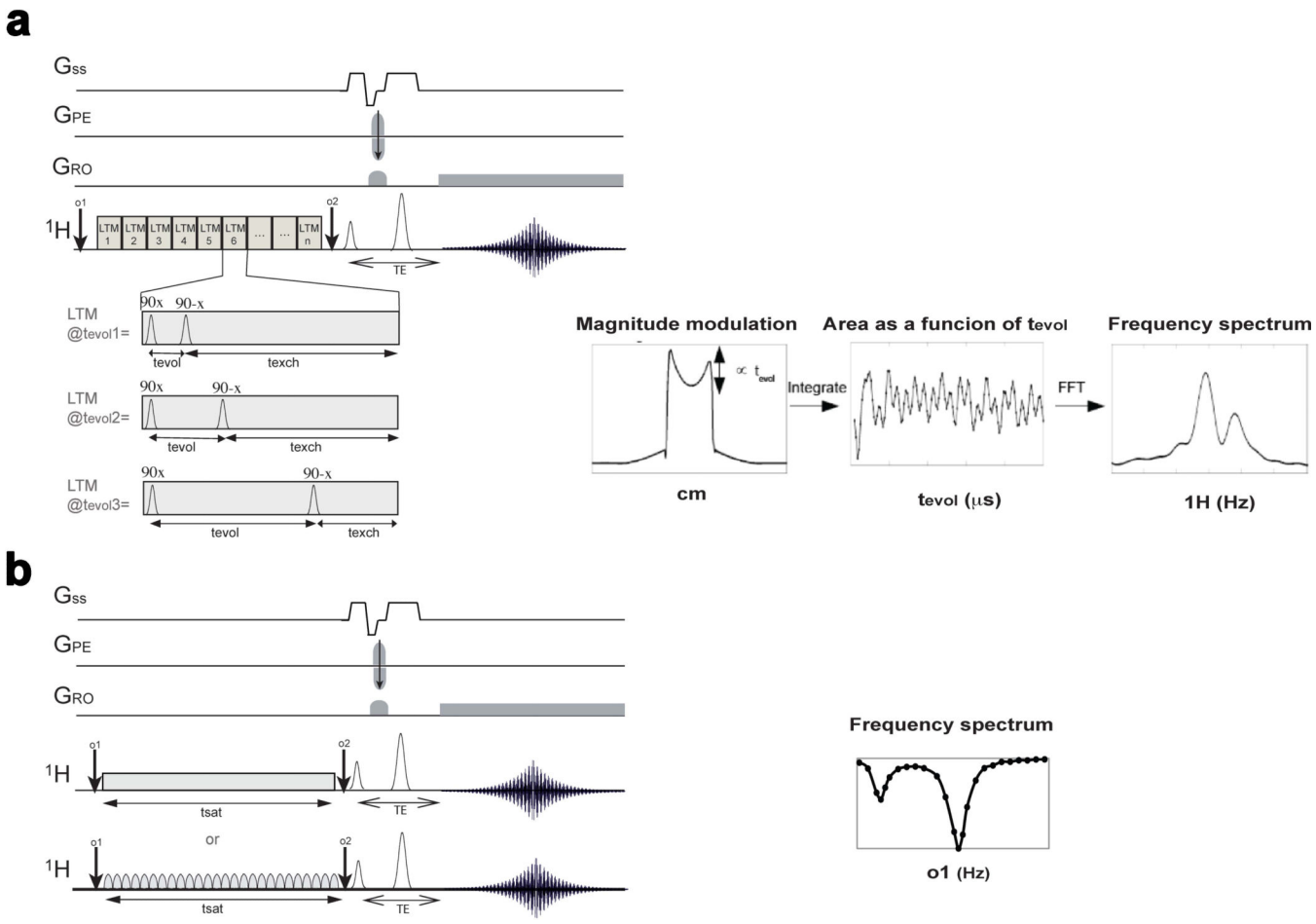

Figure 4.

Diagram depicting the differences between the FLEX sequence and standard Saturation Transfer sequence for creating frequency sensitive exchange contrast; **a)** FLEX sequence with the evolution time (t_{evol}) of the LTM's adjusted to allow frequency labeling of the modulations in water signal. The magnitude of the water signal is modulated as a function of t_{evol} through exchange transfer; **b)** Two versions of Saturation Transfer are shown: continuous wave saturation (upper panel); and pulsed saturation (lower panel); For both the o1 frequency is adjusted to provide frequency specific contrast; **c)** FLEX data can be reconstructed as a free-induction decay (FID) of amplitude PTRs containing the signal of the exchangeable protons. A Fourier transform provides the spectrum. *Reproduced from reference (73) with permission*;

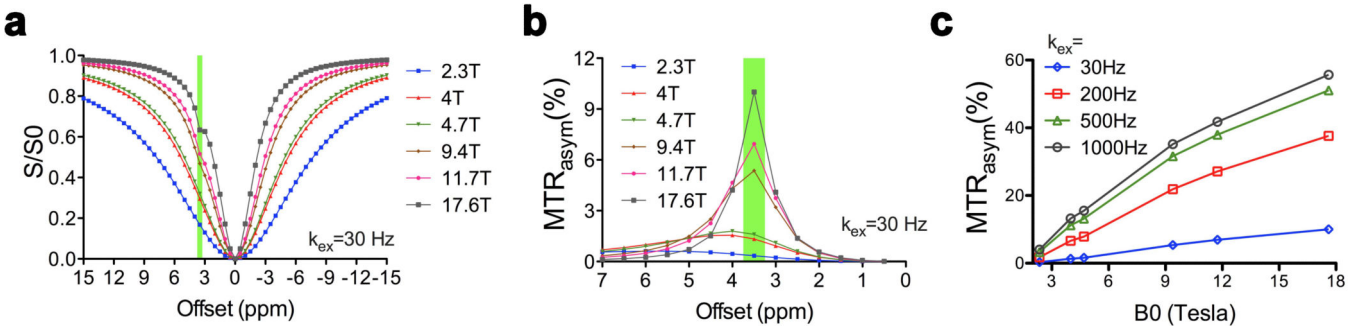

Figure 5.

Numerical simulation of B_0 field dispersion influences on CEST contrast in the mouse cortex using the Bloch equations: **a)** z spectra, **b)** MTR_{asym} plots, and **c)** peak CEST values plotted against the B_0 field with the proton exchange rate ranging from 30 Hz to 1000 Hz. The parameters for these simulation were: $\Delta\omega$ = 3.5ppm, k_{sw} = 30Hz (except for panel **c)**, B_1 = 4.7 μT (200 Hz), T1s and T2s are T1w and T2w are used as reported in the literature and listed in Table 1.

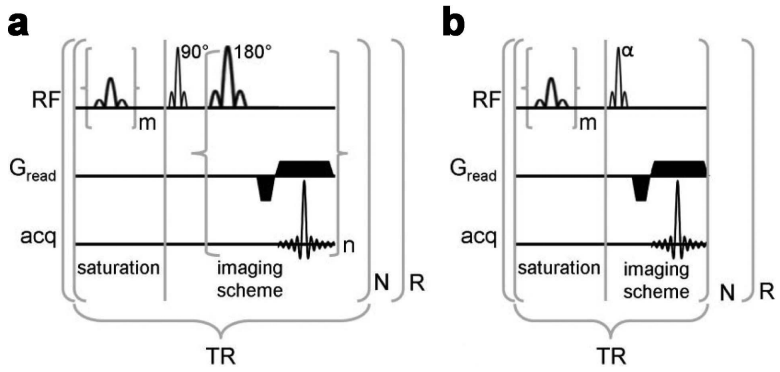

Figure 6.

Two strategies to create CEST contrast when using fast MRI sequences: **a)** Pulse sequence diagram of a PARACEST detection method with a multiple-echo imaging scheme; **b)** Pulse sequence diagram of a PARACEST detection method with a short repetitive saturation scheme. For both schemes, m represents the number of selective saturation pulses that comprise 's, and R represents the number of repetitions. For presat-RARE, n represents the number of echos that are acquired per excitation (a.k.a., RARE factor), the product of n and N represents the number of phase encoding steps, and the first lobe of G_{read} alternates in phase for each successive echo. For presat-FLASH, N represents the number of phase encoding steps. Reproduced from Fig.1 in reference (91) with permission.

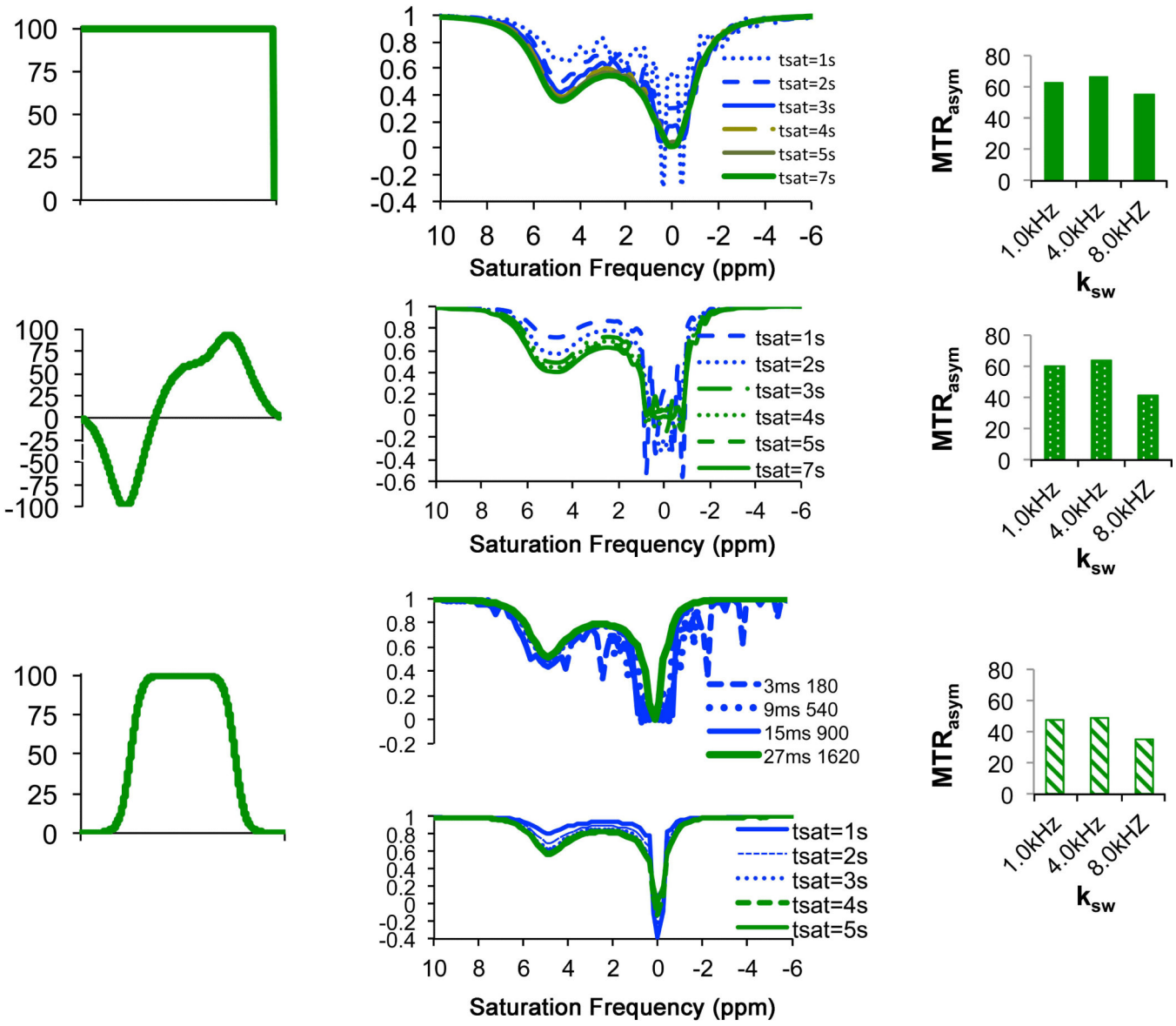

Figure 7.

Simulations of saturation transfer performance for different types of saturation pulses to illustrate some of the issues worth considering when using different waveforms. Simulations were performed setting $\Delta\omega$= 5ppm, x_{ca}=1:2000, R1w=0.25, R2w = 0.7. These were performed using the Spinevolution program. **a)** RECT Waveform, **b)** t_{sat} dependent z-spectra with k_{sw}= 1 kHz, B_1 = 10.6 μT. By t_{sat} = 4 sec, the oscillations are mostly removed; **c)** MTR_{asym} at $\Delta\omega$ = 5 ppm, t_{sat} = 7 sec,; **d)** dSNOB Waveform; **e)** t_{sat} dependent z-spectra with t_{pul} = 5 msec, θ = 180°; **f)** MTR_{asym} at $\Delta\omega$ = 5 ppm, t_{sat} =7 sec; **g**) Fermi Waveform **h)** flip angle (upper) and t_{sat} dependent with t_{pul}= 27 msec, θ = 1620° (lower) z-spectra and **i)** MTR_{asym} at $\Delta\omega$ = 5 ppm.

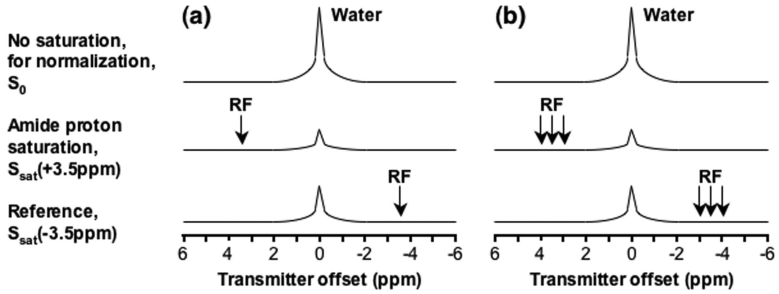

Figure 8.

Schemes for APTw image acquisition: **a)** Minimal two-offset APT scan (+3.5 ppm for label, –3.5 ppm for reference); **b)** Six-offset APT scan (±3, ±3.5, ±4 ppm). The effects of conventional MT and direct water saturation reduce the water signal intensities at all offsets (±3, ±3.5, ±4 ppm), and the existence of APT causes an extra reduction around 3.5 ppm. *Reproduced from reference (123) with permission.*

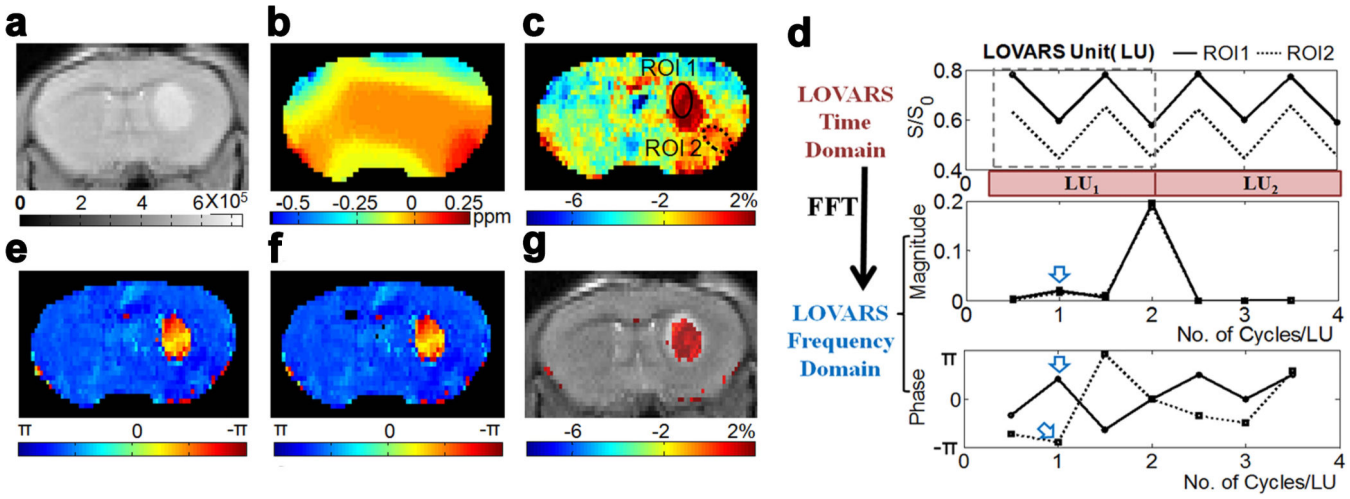

Figure 9.

In vivo demonstration of the LOVARS scheme as applied to the imaging of 9L gliosarcomas in mice. **a)** T2-w scout image; **b)** B_0 shift map (WASSR); **c)** uncorrected MTR_{asym} map; **d)** LOVARS time domain data (top) with phase (middle) and magnitude (bottom) traces determined through FFT with ROIs as marked in **c**, ROI1: tumor region and ROI2: control tissue with large B_0 shift. The arrows point to the average phase (bottom) and magnitude (middle) in ROI1 and ROI2 at 1cycle/LU based on FFT; **e)** LOVARS phase map calculated using FFT; **f)** LOVARS phase map calculated using GLM; **g)** thresholded LOVARS imaginary component map. *Reproduced from reference (125) with permission.*

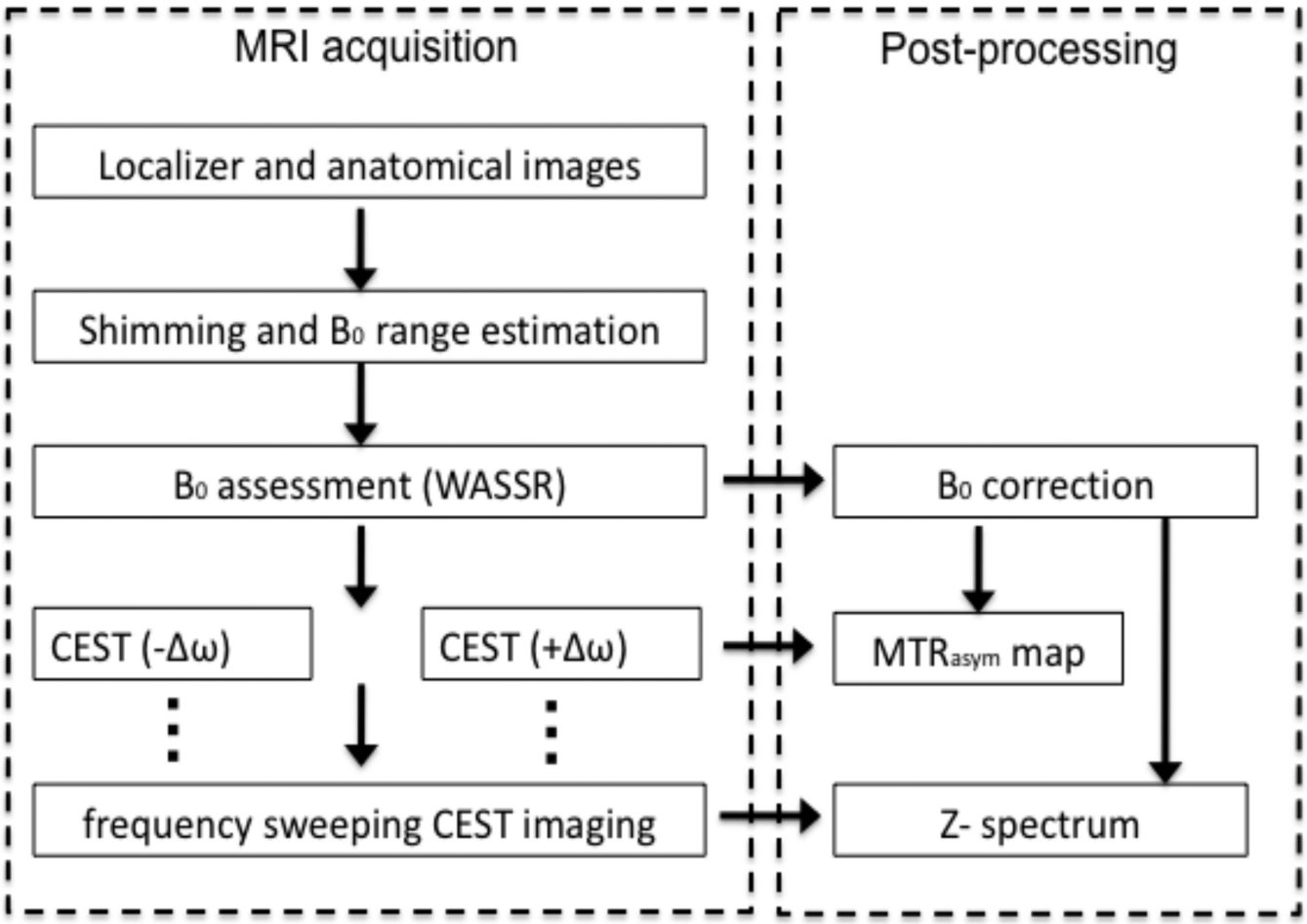

Figure 10.
Overview of a typical protocol to acquire and process CEST data. *Reproduced from reference (138) with permission.*

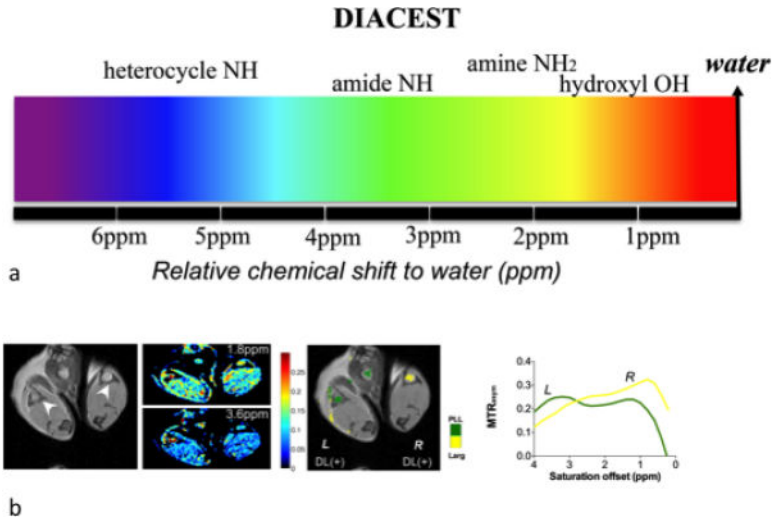

Figure 11.

a) Multicolor spectrum of DIACEST, artificial colors are assigned according to the exchangeable proton chemical shifts for a variety of diamagnetic agents, which range from 0 to 7 ppm(3); **b)** In vivo realization of the Multi-color imaging. *Reproduced from reference (3) with permission.*

Table 1

The relevant MR properties for CEST imaging of the mouse cortex at different B_0 field strengths

B_0 (Tesla)	Frequency separation (Hz) per 1 ppm	T_1 (ms)	T_2 (ms)
2.35(154)	100	1010	68.5
4(155)	170	1286	65.2
4.7(154)	200	1315	54.6
9.4(155)	400	1948	42.1
11.7(155)	500	2073	36.2
17.6(156,157)	750	2030	30

Table 2

List of fast MRI pulse sequences that have been tested for CEST studies

	Suitable Saturation schemes		Typical TR and TE		Example acquisition time per image (sec)[a]	Favorable B_0
	Single long	Short repetitive	TR (ms)	TE (ms)		
RARE(4)	+		>5000	~50[b]	24[c]	No limit[d]
FLASH(91)		+	100-300	<5	19.2[e]	No limit
EPI(51,132)	+	+	>5000	~50	40[f]	1.5T-3T
FISP(38)	+		2	½ TR	2.5[g]	1.5T-3T
3D-GRASE(103)	+		2500	200	20[h]	No limit

[a] using values in literature based on a 2D image with 64 phase encoding steps and a single average unless otherwise noted.

[b] effective TE

[c] with TR=6 sec and RARE factor =16.

[d] except it may result in high SAR at high field

[e] with TR=200ms and 32 dummy scans to reach steady state of saturation

[f] four-shot EPI with TR=10 s

[g] includes 10 dummy scans to reach steady state.

[h] With SENSE acceleration factors of 2×2 in the RL (44 steps) and SI (28 steps) directions, SE factor = 22, EPI factor = 7.